

Search for photons above 10^{18} eV by simultaneously measuring the atmospheric depth and the muon content of air showers at the Pierre Auger Observatory

A. Abdul Halim,¹ P. Abreu,² M. Aglietta,^{3,4} I. Allekotte,⁵ K. Almeida Cheminant,^{6,7,8} A. Almela,^{9,10} R. Aloisio,^{11,12} J. Alvarez-Muñiz,¹³ J. Ammerman Yebra,¹³ G.A. Anastasi,^{14,15} L. Anchordoqui,¹⁶ B. Andrada,⁹ L. Andrade Dourado,^{11,12} S. Andringa,² L. Apollonio,^{17,18} C. Aramo,¹⁹ P.R. Araújo Ferreira,²⁰ E. Arnone,^{21,4} J.C. Arteaga Velázquez,²² P. Assis,² G. Avila,²³ E. Avocone,^{24,12} A. Bakalova,²⁵ F. Barbato,^{11,12} A. Bartz Mocellin,²⁶ C. Berat,²⁷ M.E. Bertaina,^{21,4} G. Bhatta,⁸ M. Bianciotto,^{21,4} P.L. Biermann,²⁸ V. Binet,²⁹ K. Bismark,^{30,9} T. Bister,^{7,6} J. Biteau,^{31,32} J. Blazek,²⁵ C. Bleve,²⁷ J. Blümer,³³ M. Boháčová,²⁵ D. Boncioli,^{24,12} C. Bonifazi,³⁴ L. Bonneau Arbeletche,³⁵ N. Borodai,⁸ J. Brack,³⁶ P.G. Bricchetto Orchera,⁹ F.L. Briechle,²⁰ A. Bueno,³⁷ S. Buitink,³⁸ M. Buscemi,^{15,14} M. Büskén,^{30,9} A. Bwembya,^{7,6} K.S. Caballero-Mora,³⁹ S. Cabana-Freire,¹³ L. Caccianiga,^{17,18} F. Campuzano,⁴⁰ R. Caruso,^{14,15} A. Castellina,^{3,4} F. Catalani,⁴¹ G. Cataldi,⁴² L. Cazon,¹³ M. Cerda,⁴³ B. Čermáková,³³ A. Cermenati,^{11,12} J.A. Chinellato,³⁵ J. Chudoba,²⁵ L. Chytka,⁴⁴ R.W. Clay,¹ A.C. Cobos Cerutti,⁴⁰ R. Colalillo,^{45,19} M.R. Coluccia,⁴² R. Conceição,² A. Condorelli,³¹ G. Consolati,^{18,46} M. Conte,^{47,42} F. Convenga,^{24,12} D. Correia dos Santos,⁴⁸ P.J. Costa,² C.E. Covault,⁴⁹ M. Cristinziani,⁵⁰ C.S. Cruz Sanchez,⁵¹ S. Dasso,^{52,53} K. Daumiller,³³ B.R. Dawson,¹ R.M. de Almeida,⁴⁸ B. de Errico,⁴⁸ J. de Jesús,^{9,33} S.J. de Jong,^{7,6} J.R.T. de Mello Neto,⁴⁸ I. De Mitri,^{11,12} J. de Oliveira,⁵⁴ D. de Oliveira Franco,⁴² F. de Palma,^{47,42} V. de Souza,⁵⁵ E. De Vito,^{47,42} A. Del Popolo,^{14,15} O. Deligny,⁵⁶ N. Denner,²⁵ L. Deval,^{33,9} A. di Matteo,⁴ J.A. do,^{1,57} M. Dobre,⁵⁸ C. Dobrigkeit,³⁵ J.C. D’Olivo,⁵⁹ L.M. Domingues Mendes,^{60,2} Q. Dorosti,⁵⁰ J.C. dos Anjos,⁶⁰ R.C. dos Anjos,⁶¹ J. Ebr,²⁵ F. Ellwanger,³³ M. Emam,^{7,6} R. Engel,^{30,33} I. Epicoco,^{47,42} M. Erdmann,²⁰ A. Etchegoyen,^{9,10} C. Evoli,^{11,12} H. Falcke,^{7,62,6} G. Farrar,⁶³ A.C. Fauth,³⁵ T. Fehler,⁵⁰ F. Feldbusch,⁶⁴ F. Fenu,^{33,65} A. Fernandes,² B. Fick,⁶⁶ J.M. Figueira,⁹ P. Filip,^{30,9} A. Filipčič,^{67,68} T. Fitoussi,³³ B. Flaggs,⁶⁹ T. Fodran,⁷ T. Fujii,^{70,71} A. Fuster,^{9,10} C. Galea,⁷ B. García,⁴⁰ C. Gaudu,⁷² A. Gherghel-Lascu,⁵⁸ P.L. Ghia,⁵⁶ U. Giaccari,⁴² J. Glombitza,^{20,73} F. Gobbi,⁴³ F. Gollan,⁹ G. Golup,⁵ M. Gómez Berisso,⁵ P.F. Gómez Vitale,²³ J.P. Gongora,²³ J.M. González,⁵ N. González,⁹ D. Góra,⁸ A. Gorgi,^{3,4} M. Gottowik,³³ F. Guarino,^{45,19} G.P. Guedes,⁷⁴ E. Guido,⁵⁰ L. Gülzow,³³ S. Hahn,³⁰ P. Hamal,²⁵ M.R. Hampel,⁹ P. Hansen,⁵¹ D. Harari,⁵ V.M. Harvey,¹ A. Haungs,³³ T. Hebbeker,²⁰ C. Hojvat,⁷⁵ J.R. Hörandel,^{7,6} P. Horvath,⁴⁴ M. Hrabovský,⁴⁴ T. Huege,^{33,38} A. Insolia,^{14,15} P.G. Isar,⁷⁶ P. Janecek,²⁵ V. Jilek,²⁵ J.A. Johnsen,²⁶ J. Jurysek,²⁵ K.-H. Kampert,⁷² B. Keilhauer,³³ A. Khakurdikar,⁷ V.V. Kizakke Covilakam,^{9,33} H.O. Klages,³³ M. Kleifges,⁶⁴ F. Knapp,³⁰ J. Köhler,³³ F. Krieger,²⁰ N. Kunka,⁶⁴ B.L. Lago,⁷⁷ N. Langner,²⁰ M.A. Leigui de Oliveira,⁷⁸ Y. Lema-Capeans,¹³ A. Letessier-Selvon,⁷⁹ I. Lhenry-Yvon,⁵⁶ L. Lopes,² L. Lu,⁸⁰ Q. Luce,³⁰ J.P. Lundquist,⁶⁸ A. Machado Payeras,³⁵ M. Majercakova,²⁵ D. Mandat,²⁵ B.C. Manning,¹ P. Mantsch,⁷⁵ F.M. Mariani,^{17,18} A.G. Mariazzi,⁵¹ I.C. Mariş,⁸¹ G. Marsella,^{82,15} D. Martello,^{47,42} S. Martinelli,^{33,9} O. Martínez Bravo,⁸³ M.A. Martins,¹³ H.-J. Mathes,³³ J. Matthews,⁸⁴ G. Matthiae,^{85,86} E. Mayotte,²⁶ S. Mayotte,²⁶ P.O. Mazur,⁷⁵ G. Medina-Tanco,⁵⁹ J. Meinert,⁷² D. Melo,⁹ A. Menshikov,⁶⁴ C. Merx,³³ S. Michal,²⁵ M.I. Micheletti,²⁹ L. Miramonti,^{17,18} S. Mollerach,⁵ F. Montanet,²⁷ L. Morejon,⁷² K. Mulrey,^{7,6} R. Mussa,⁴ W.M. Namasaka,⁷² S. Negi,²⁵ L. Nellen,⁵⁹ K. Nguyen,⁶⁶ G. Nicora,⁸⁷ M. Niechciol,⁵⁰ D. Nitz,⁶⁶ D. Nosek,⁸⁸ V. Novotny,⁸⁸ L. Nožka,⁴⁴ A. Nucita,^{47,42} L.A. Núñez,⁸⁹ C. Oliveira,⁵⁵ M. Palatka,²⁵ J. Pallotta,⁸⁷ S. Panja,²⁵ G. Parente,¹³ T. Paulsen,⁷² J. Pawlowsky,⁷² M. Pech,²⁵ J. Pękala,⁸ R. Pelayo,⁹⁰ V. Pelgrims,⁸¹ L.A.S. Pereira,⁹¹ E.E. Pereira Martins,^{30,9} C. Pérez Bertolli,^{9,33} L. Perrone,^{47,42} S. Petrerá,^{11,12} C. Petrucci,²⁴ T. Pierog,³³ M. Pimenta,² M. Platino,⁹ B. Pont,⁷ M. Pothast,^{6,7} M. Pourmohammad Shahvar,^{82,15} P. Privitera,⁷⁰ M. Prouza,²⁵ S. Querschfeld,⁷² J. Rautenberg,⁷² D. Ravignani,⁹ J.V. Reginatto Akim,³⁵ M. Reininghaus,³⁰ A. Reuzki,²⁰ J. Ridky,²⁵ F. Riehn,¹³ M. Risse,⁵⁰ V. Rizi,^{24,12} W. Rodrigues de Carvalho,⁷ E. Rodriguez,^{9,33} J. Rodriguez Rojo,²³ M.J. Roncoroni,⁹ S. Rossoni,⁹² M. Roth,³³ E. Roulet,⁵ A.C. Rovero,⁵² A. Saftoiu,⁵⁸ M. Saharan,⁷ F. Salamida,^{24,12} H. Salazar,⁸³ G. Salina,⁸⁶ J.D. Sanabria Gomez,⁸⁹ F. Sánchez,⁹ E.M. Santos,⁹³ E. Santos,²⁵ F. Sarazin,²⁶ R. Sarmiento,² R. Sato,²³ P. Savina,⁸⁰ C.M. Schäfer,³⁰ V. Scherini,^{47,42} H. Schieler,³³ M. Schimassek,⁵⁶ M. Schimp,⁷² D. Schmidt,³³ O. Scholten,^{38,94} H. Schoorlemmer,^{7,6} P. Schovánek,²⁵ F.G. Schröder,^{69,33} J. Schulte,²⁰ T. Schulz,³³ S.J. Sciutto,⁵¹ M. Scornavacche,^{9,33} A. Sedoski,⁹ A. Segreto,^{95,15} S. Sehgal,⁷² S.U. Shivashankara,⁶⁸ G. Sigl,⁹² K. Simkova,^{38,81} F. Simon,⁶⁴ R. Smau,⁵⁸ R. Šmída,⁷⁰ P. Sommers,⁹⁶ R. Squartini,⁴³ M. Stadelmaier,^{18,17,33} S. Stanič,⁶⁸ J. Stasielak,⁸ P. Stassi,²⁷ S. Strähnz,³⁰ M. Straub,²⁰ T. Suomijärvi,³¹ A.D. Supanitsky,⁹ Z. Svozilikova,²⁵ Z. Szadkowski,⁹⁷ F. Tairli,¹ A. Tapia,⁹⁸ C. Taricco,^{21,4} C. Timmermans,^{6,7} O. Tkachenko,²⁵ P. Tobiska,²⁵ C.J. Todero Peixoto,⁴¹ B. Tomé,² Z. Torrès,²⁷ A. Travaini,⁴³ P. Travnicek,²⁵ M. Tueros,⁵¹ M. Unger,³³ R. Uzeiroska,⁷² L. Vaclavek,⁴⁴ M. Vacula,⁴⁴ J.F. Valdés Galicia,⁵⁹ L. Valore,^{45,19} E. Varela,⁸³ V. Vašíčková,⁷² A. Vásquez-Ramírez,⁸⁹ D. Veberič,³³ I.D. Vergara Quispe,⁵¹ V. Verzi,⁸⁶ J. Vicha,²⁵ J. Vink,⁹⁹ S. Vorobiov,⁶⁸ C. Watanabe,⁴⁸ A.A. Watson,¹⁰⁰ A. Weindl,³³ L. Wiencke,²⁶ H. Wilczyński,⁸ D. Wittkowski,⁷² B. Wundheiler,⁹ B. Yue,⁷² A. Yushkov,²⁵ O. Zapparrata,⁸¹ E. Zas,¹³ D. Zavrtnik,^{68,67} and M. Zavrtnik^{67,68}

(The Pierre Auger Collaboration)*

¹University of Adelaide, Adelaide, S.A., Australia

- ²Laboratório de Instrumentação e Física Experimental de Partículas – LIP and Instituto Superior Técnico – IST, Universidade de Lisboa – UL, Lisboa, Portugal
- ³Osservatorio Astrofisico di Torino (INAF), Torino, Italy
- ⁴INFN, Sezione di Torino, Torino, Italy
- ⁵Centro Atómico Bariloche and Instituto Balseiro (CNEA-UNCuyo-CONICET), San Carlos de Bariloche, Argentina
- ⁶Nationaal Instituut voor Kernfysica en Hoge Energie Fysica (NIKHEF), Science Park, Amsterdam, The Netherlands
- ⁷IMAPP, Radboud University Nijmegen, Nijmegen, The Netherlands
- ⁸Institute of Nuclear Physics PAN, Krakow, Poland
- ⁹Instituto de Tecnologías en Detección y Astropartículas (CNEA, CONICET, UNSAM), Buenos Aires, Argentina
- ¹⁰Universidad Tecnológica Nacional – Facultad Regional Buenos Aires, Buenos Aires, Argentina
- ¹¹Gran Sasso Science Institute, L'Aquila, Italy
- ¹²INFN Laboratori Nazionali del Gran Sasso, Assergi (L'Aquila), Italy
- ¹³Instituto Galego de Física de Altas Enerxías (IGFAE), Universidade de Santiago de Compostela, Santiago de Compostela, Spain
- ¹⁴Università di Catania, Dipartimento di Fisica e Astronomia “Ettore Majorana”, Catania, Italy
- ¹⁵INFN, Sezione di Catania, Catania, Italy
- ¹⁶Department of Physics and Astronomy, Lehman College, City University of New York, Bronx, NY, USA
- ¹⁷Università di Milano, Dipartimento di Fisica, Milano, Italy
- ¹⁸INFN, Sezione di Milano, Milano, Italy
- ¹⁹INFN, Sezione di Napoli, Napoli, Italy
- ²⁰RWTH Aachen University, III. Physikalisches Institut A, Aachen, Germany
- ²¹Università Torino, Dipartimento di Fisica, Torino, Italy
- ²²Universidad Michoacana de San Nicolás de Hidalgo, Morelia, Michoacán, México
- ²³Observatorio Pierre Auger and Comisión Nacional de Energía Atómica, Malargüe, Argentina
- ²⁴Università dell'Aquila, Dipartimento di Scienze Fisiche e Chimiche, L'Aquila, Italy
- ²⁵Institute of Physics of the Czech Academy of Sciences, Prague, Czech Republic
- ²⁶Colorado School of Mines, Golden, CO, USA
- ²⁷Univ. Grenoble Alpes, CNRS, Grenoble Institute of Engineering Univ. Grenoble Alpes, LPSC-IN2P3, 38000 Grenoble, France
- ²⁸Max-Planck-Institut für Radioastronomie, Bonn, Germany
- ²⁹Instituto de Física de Rosario (IFIR) – CONICET/U.N.R. and Facultad de Ciencias Bioquímicas y Farmacéuticas U.N.R., Rosario, Argentina
- ³⁰Karlsruhe Institute of Technology (KIT), Institute for Experimental Particle Physics, Karlsruhe, Germany
- ³¹Université Paris-Saclay, CNRS/IN2P3, IJCLab, Orsay, France
- ³²Institut universitaire de France (IUF), France
- ³³Karlsruhe Institute of Technology (KIT), Institute for Astroparticle Physics, Karlsruhe, Germany
- ³⁴International Center of Advanced Studies and Instituto de Ciencias Físicas, ECyT-UNSAM and CONICET, Campus Miguelete – San Martín, Buenos Aires, Argentina
- ³⁵Universidade Estadual de Campinas (UNICAMP), IFGW, Campinas, SP, Brazil
- ³⁶Colorado State University, Fort Collins, CO, USA
- ³⁷Universidad de Granada and C.A.F.P.E., Granada, Spain
- ³⁸Vrije Universiteit Brussels, Brussels, Belgium
- ³⁹Universidad Autónoma de Chiapas, Tuxtla Gutiérrez, Chiapas, México
- ⁴⁰Instituto de Tecnologías en Detección y Astropartículas (CNEA, CONICET, UNSAM), and Universidad Tecnológica Nacional – Facultad Regional Mendoza (CONICET/CNEA), Mendoza, Argentina
- ⁴¹Universidade de São Paulo, Escola de Engenharia de Lorena, Lorena, SP, Brazil
- ⁴²INFN, Sezione di Lecce, Lecce, Italy
- ⁴³Observatorio Pierre Auger, Malargüe, Argentina
- ⁴⁴Palacky University, Olomouc, Czech Republic
- ⁴⁵Università di Napoli “Federico II”, Dipartimento di Fisica “Ettore Pancini”, Napoli, Italy
- ⁴⁶Politecnico di Milano, Dipartimento di Scienze e Tecnologie Aerospaziali, Milano, Italy
- ⁴⁷Università del Salento, Dipartimento di Matematica e Fisica “E. De Giorgi”, Lecce, Italy
- ⁴⁸Universidade Federal do Rio de Janeiro, Instituto de Física, Rio de Janeiro, RJ, Brazil
- ⁴⁹Case Western Reserve University, Cleveland, OH, USA
- ⁵⁰Universität Siegen, Department Physik – Experimentelle Teilchenphysik, Siegen, Germany
- ⁵¹IFLP, Universidad Nacional de La Plata and CONICET, La Plata, Argentina
- ⁵²Instituto de Astronomía y Física del Espacio (IAFE, CONICET-UBA), Buenos Aires, Argentina
- ⁵³Departamento de Física and Departamento de Ciencias de la Atmósfera y los Océanos, FCEyN, Universidad de Buenos Aires and CONICET, Buenos Aires, Argentina
- ⁵⁴Instituto Federal de Educação, Ciência e Tecnologia do Rio de Janeiro (IFRJ), Brazil
- ⁵⁵Universidade de São Paulo, Instituto de Física de São Carlos, São Carlos, SP, Brazil
- ⁵⁶CNRS/IN2P3, IJCLab, Université Paris-Saclay, Orsay, France
- ⁵⁷Universidad Nacional de San Agustín de Arequipa, Facultad de Ciencias Naturales y Formales, Arequipa, Peru
- ⁵⁸“Horia Hulubei” National Institute for Physics and Nuclear Engineering, Bucharest-Magurele, Romania
- ⁵⁹Universidad Nacional Autónoma de México, México, D.F., México
- ⁶⁰Centro Brasileiro de Pesquisas Físicas, Rio de Janeiro, RJ, Brazil

- ⁶¹Universidade Federal do Paraná, Setor Palotina, Palotina, Brazil
- ⁶²Stichting Astronomisch Onderzoek in Nederland (ASTRON), Dwingeloo, The Netherlands
- ⁶³New York University, New York, NY, USA
- ⁶⁴Karlsruhe Institute of Technology (KIT), Institut für Prozessdatenverarbeitung und Elektronik, Karlsruhe, Germany
- ⁶⁵now at Agenzia Spaziale Italiana (ASI), Via del Politecnico 00133, Roma, Italy
- ⁶⁶Michigan Technological University, Houghton, MI, USA
- ⁶⁷Experimental Particle Physics Department, J. Stefan Institute, Ljubljana, Slovenia
- ⁶⁸Center for Astrophysics and Cosmology (CAC), University of Nova Gorica, Nova Gorica, Slovenia
- ⁶⁹University of Delaware, Department of Physics and Astronomy, Bartol Research Institute, Newark, DE, USA
- ⁷⁰University of Chicago, Enrico Fermi Institute, Chicago, IL, USA
- ⁷¹now at Graduate School of Science, Osaka Metropolitan University, Osaka, Japan
- ⁷²Bergische Universität Wuppertal, Department of Physics, Wuppertal, Germany
- ⁷³now at ECAP, Erlangen, Germany
- ⁷⁴Universidade Estadual de Feira de Santana, Feira de Santana, Brazil
- ⁷⁵Fermi National Accelerator Laboratory, Fermilab, Batavia, IL, USA
- ⁷⁶Institute of Space Science, Bucharest-Magurele, Romania
- ⁷⁷Centro Federal de Educação Tecnológica Celso Suckow da Fonseca, Petropolis, Brazil
- ⁷⁸Universidade Federal do ABC, Santo André, SP, Brazil
- ⁷⁹Laboratoire de Physique Nucléaire et de Hautes Energies (LPNHE), Sorbonne Université, Université de Paris, CNRS-IN2P3, Paris, France
- ⁸⁰University of Wisconsin-Madison, Department of Physics and WIPAC, Madison, WI, USA
- ⁸¹Université Libre de Bruxelles (ULB), Brussels, Belgium
- ⁸²Università di Palermo, Dipartimento di Fisica e Chimica "E. Segrè", Palermo, Italy
- ⁸³Benemérita Universidad Autónoma de Puebla, Puebla, México
- ⁸⁴Louisiana State University, Baton Rouge, LA, USA
- ⁸⁵Università di Roma "Tor Vergata", Dipartimento di Fisica, Roma, Italy
- ⁸⁶INFN, Sezione di Roma "Tor Vergata", Roma, Italy
- ⁸⁷Laboratorio Atmósfera – Departamento de Investigaciones en Láseres y sus Aplicaciones – UNIDEF (CITEDEF-CONICET), Argentina
- ⁸⁸Charles University, Faculty of Mathematics and Physics, Institute of Particle and Nuclear Physics, Prague, Czech Republic
- ⁸⁹Universidad Industrial de Santander, Bucaramanga, Colombia
- ⁹⁰Unidad Profesional Interdisciplinaria en Ingeniería y Tecnologías Avanzadas del Instituto Politécnico Nacional (UPIITA-IPN), México, D.F., México
- ⁹¹Universidade Federal de Campina Grande, Centro de Ciências e Tecnologia, Campina Grande, Brazil
- ⁹²Universität Hamburg, II. Institut für Theoretische Physik, Hamburg, Germany
- ⁹³Universidade de São Paulo, Instituto de Física, São Paulo, SP, Brazil
- ⁹⁴also at Kapteyn Institute, University of Groningen, Groningen, The Netherlands
- ⁹⁵Istituto di Astrofisica Spaziale e Fisica Cosmica di Palermo (INAF), Palermo, Italy
- ⁹⁶Pennsylvania State University, University Park, PA, USA
- ⁹⁷University of Łódź, Faculty of High-Energy Astrophysics, Łódź, Poland
- ⁹⁸Universidad de Medellín, Medellín, Colombia
- ⁹⁹Universiteit van Amsterdam, Faculty of Science, Amsterdam, The Netherlands
- ¹⁰⁰School of Physics and Astronomy, University of Leeds, Leeds, United Kingdom
- (Dated: June 12, 2024)

The Pierre Auger Observatory is the most sensitive instrument to detect photons with energies above 10^{17} eV. It measures extensive air showers generated by ultra high energy cosmic rays using a hybrid technique that exploits the combination of a fluorescence detector with a ground array of particle detectors. The signatures of a photon-induced air shower are a larger atmospheric depth of the shower maximum (X_{\max}) and a steeper lateral distribution function, along with a lower number of muons with respect to the bulk of hadron-induced cascades. In this work, a new analysis technique in the energy interval between 1 and 30 EeV ($1 \text{ EeV} = 10^{18} \text{ eV}$) has been developed by combining the fluorescence detector-based measurement of X_{\max} with the specific features of the surface detector signal through a parameter related to the air shower muon content, derived from the universality of the air shower development. No evidence of a statistically significant signal due to photon primaries was found using data collected in about 12 years of operation. Thus, upper bounds to the integral photon flux have been set using a detailed calculation of the detector exposure, in combination with a data-driven background estimation. The derived 95% confidence level upper limits are 0.0403, 0.01113, 0.0035, 0.0023, and 0.0021 $\text{km}^{-2} \text{sr}^{-1} \text{yr}^{-1}$ above 1, 2, 3, 5, and 10 EeV, respectively, leading to the most stringent upper limits on the photon flux in the EeV range. Compared with past results, the upper limits were improved by about 40% for the lowest energy threshold and by a factor 3 above 3 EeV, where no candidates were found and the expected background is negligible. The presented limits can be used to probe the assumptions on chemical composition of ultra-high energy cosmic rays and allow for the constraint of the mass and lifetime phase space of super-heavy dark matter particles.

I. INTRODUCTION

Photons with energy higher than $1 \text{ EeV} = 10^{18} \text{ eV}$ are expected to be produced by ultra-high energy cosmic rays (UHECRs) in interactions with the microwave background radiation during their propagation to Earth, via the Greisen-Zatsepin-Kuzmin effect [1, 2]. The produced photons may, in turn, interact with the soft photons of the extra-galactic background light (EBL), resulting in a flux significantly lower than that of UHECRs by orders of magnitude and limiting the explored horizon to a few Mpc [3]. Nevertheless implications of the search for EeV photons remain relevant for both cosmic-ray and fundamental physics. Unlike charged cosmic rays, which are deflected by the magnetic fields permeating the Universe, photons point back to their sources. Therefore, the quest for the origin of UHECRs benefits from a multi-messenger approach, since direct information about their acceleration sites can be obtained by searching for the neutral particles, photons and neutrinos, generated by the interactions of cosmic rays at the acceleration sites, via the so-called *astrophysical beam dump* process [4, 5]. Cosmogenic photons can also probe UHECRs as their flux depends on the characteristics of the sources, as well as on the nature of the parent nuclei. Finally, EeV photons might probe new physics, as their detection would be a smoking gun for dark matter composed of super-heavy particles decaying to photons or other exotic scenarios [6–8].

Due to the weakness of both the cosmic-ray and cosmic-photon fluxes, the photon search can presently only be done through large ground-based detectors that exploit the phenomenon of extensive air showers. The identification of photon primaries relies on the ability to distinguish the showers generated by photons from those initiated by the overwhelming background of protons and heavier nuclei. Since the radiation length in the atmosphere is more than two orders of magnitude smaller than the mean free path for photo-nuclear interaction in the ultra-high energy range, in photon showers the transfer of energy to the hadron/muon channel is much smaller than in hadron-induced air-showers, resulting in a lower number of secondary muons. Additionally, as the development of photon showers is delayed by the typically small multiplicity of electromagnetic interactions and even further in the EeV energy range due to the LPM effect [9], the depth of the shower maximum, X_{max} , is deeper in the atmosphere with respect to showers initiated by hadrons.

In this work, a search for photons at energies above 1 EeV using the Auger data is presented. The paper is structured as follows: **Section II** provides a brief description of the Pierre Auger Observatory and of its hybrid operating mode, combining a Surface Detector array (SD) with a Fluorescence Detector (FD). In **Section III**, we will introduce a new method for calculating a parameter, F_{μ} , related to the muonic component of an air shower. The method is based on air shower universality in combination with the high-quality reconstruction of hybrid events, simultaneously observed by the FD and

the SD. The analysis is applied to 12 years of high-quality selected data, as discussed in **Section IV**. To fully exploit the hybrid approach, F_{μ} is combined with the depth of the shower maximum, X_{max} , measured by the Fluorescence Detector of the Pierre Auger Observatory in a Fisher discriminant analysis in **Section V**. The expected background resulting from hadron-like showers is examined in **Section VI**. The result of the application of the selection strategy to data is detailed in **Section VII**. In the absence of any significant signal, we establish upper limits on the integral photon flux, which are presented in **Section VIII**, along with their associated systematic uncertainties. Finally, the implications of the derived results are briefly discussed in **Section IX**.

II. THE PIERRE AUGER OBSERVATORY

The Pierre Auger Observatory [10], located near the town of Malargüe in the Argentinian *Pampa Amarilla*, is the largest cosmic-ray observatory to date, offering an unprecedented exposure to EeV photons. A key feature of the Pierre Auger Observatory is its hybrid concept, based on the combination of measurements provided by a surface detector array and a fluorescence detector. The surface detector consists of 1600 water-Cherenkov detector (WCD) stations arranged on a triangular grid with a spacing of 1500 m, covering a total area of about 3000 km².

The SD samples the shower density at ground level, i.e., the distribution of particles as a function of the distance from the shower axis, with a duty cycle of 100%. Moreover the time profiles of the signals recorded with the WCDs can be used to build observables which are sensitive to the nature of the primary cosmic ray. The SD is overlooked by 27 fluorescence telescopes, located at four sites at the border of the array, with field of view of $30^{\circ} \times 30^{\circ}$. The FD records the longitudinal shower development in the atmosphere above the SD and it can only be operated during clear, moonless nights, reducing the duty cycle to 15%. The FD provides a direct observation of the longitudinal shower profile, which allows for the measurement of the energy, E , and of the X_{max} of a shower. Each fluorescence telescope hosts a camera of 440 photomultipliers (pixels). The pattern of triggered pixels in the telescopes along with their trigger times are used to reconstruct the geometry of the incoming showers. At this level, the temporal information provided by even a single station of the SD can greatly improve the accuracy in determining the shower direction and its impact point at the ground (hereafter named as core). Once the geometry is reconstructed, the energy deposited in the atmosphere by secondary particles can be derived through the measurement of the fluorescence light emitted by nitrogen molecules during the passage of the shower through the atmosphere. This is done by making use of the optical properties of the atmosphere provided by several instruments continuously monitoring the volume over the array, as described in [11, 12]. The energy of the primary particle is finally derived in a calorimetric way as the integral of the fit of a modified Gaisser-Hillas function to the observed longitudinal profile [13, 14], and corrected for the invisible energy

* spokespersons@auger.org; <http://www.auger.org>

fraction carried by neutrinos and muons by following a data driven approach [15].

III. SEARCH FOR PHOTONS IN THE CONTEXT OF AIR SHOWER UNIVERSALITY

In this work, we will perform the photon-identification using hybrid events, i.e., events detected by the FD in combination with the SD. The main signature of a photon-induced air shower is a larger atmospheric depth at the shower maximum and a lower number of muons than the bulk of hadron-induced background. In Fig. 1, the distributions of X_{\max} and the number of muons are shown for simulated air showers initiated by proton (red), photon (blue) and iron (black) primaries at 1 EeV and 10 EeV. Photon-initiated showers are well separated from showers initiated by hadrons in both cases. CONEX [16] air-shower generator was used for this plot.

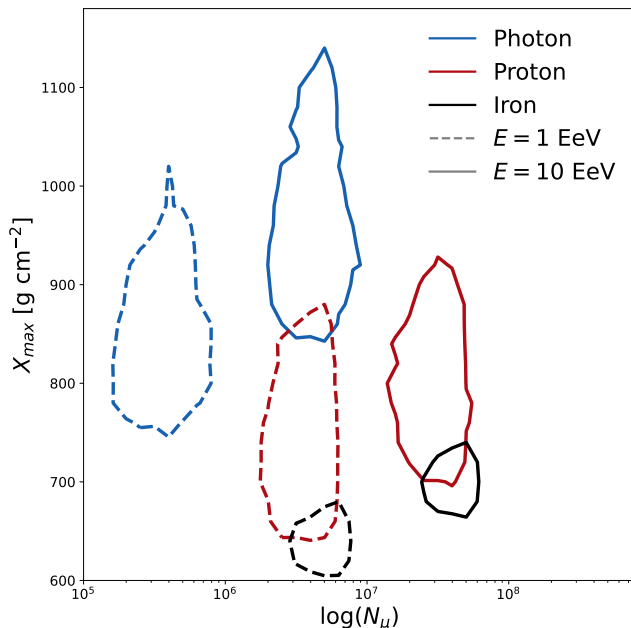


Figure 1. X_{\max} and number of muons distributions for simulated air shower initiated by proton- (red) photon- (blue) iron- (black) primaries, at 1 EeV (dashed) and 10 EeV (solid). Contour lines enclose the 90% of the distribution for each primary type. The CONEX [16] air-shower generator was used for this plot.

Although the SD observes showers at a fixed depth, the specific characteristics of the longitudinal development and the relative weight of shower particle components are embedded in the detected signals. To extract this information, we developed a new variable, F_{μ} , related to the muonic content of the shower, derived in the context of air shower universality. The general idea behind air shower universality is that the energy spectrum of the secondary particles produced during the shower development, as well as their angular and lateral distributions, depend only on the energy of the primary and on the stage of the shower development [17, 18]. Thus the average

properties of an EAS can be described by a few macroscopic shower characteristics. In general, for a given detector, it is possible to predict the signal produced by secondary particles at the different stages of the shower development. For the specific case of the SD detector, the total signal in each WCD can be modelled as the superposition of four components: S_{μ} for muons, $S_{e\gamma}$ for e^{\pm} and γ from high-energy pions, $S_{e\gamma(\mu)}$ for e^{\pm} and γ from muon decays, $S_{e\gamma(\text{had})}$ for e^{\pm} and γ due to low-energy hadrons. A parameterisation of each signal component for the WCD of the Pierre Auger Observatory was derived in [19, 20]. The relative contributions of the described four components to the expected overall signal of a surface detector station are visualized in Fig. 2 for an exemplary simulated proton of about 30 EeV. The predicted total signal, S_{pred} , can be expressed as

$$S_{\text{pred}} = \sum_{i=1}^4 S_i = \sum_{i=1}^4 f_i(F_{\mu}) S_{i,\text{comp}} \quad (1)$$

where i runs over the four components, $S_{i,\text{comp}}$ is the signal of each component that, according to the universality model, depends only on the primary total energy E , on X_{\max} , and on the geometry of the shower. The dependence on the mass of the primary particle is factorized and entirely contained in the terms denoted as f_i .

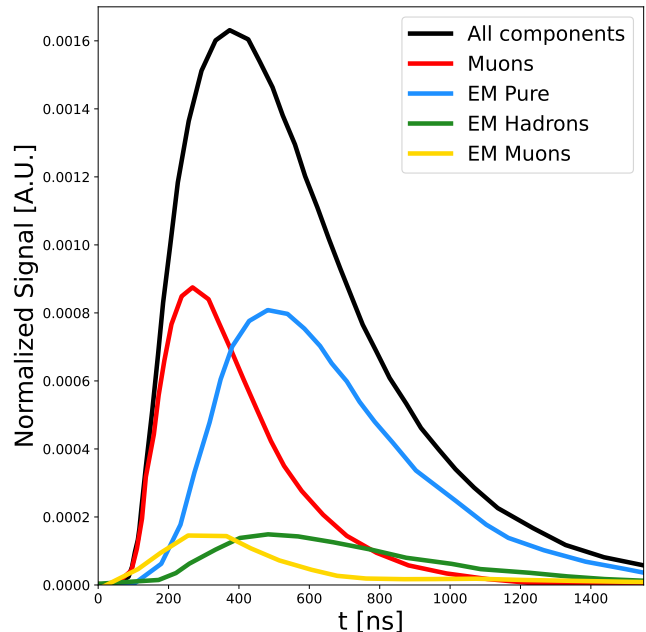


Figure 2. Conceptual visualization of the surface detector signal components as a function of time, according to the universality paradigm [20].

More specifically, the variable F_{μ} is defined as the ratio of the signal due to the muonic contribution S_{μ} , and its reference value $S_{\mu,\text{ref}}$ calculated for a proton-induced shower in a way that a value of F_{μ} significantly less than one is indicative of a large deviation from a hadronic shower.

The proposed method aims at maximizing the benefit of combining the predictive power of the universality model with

the accuracy in the determination of E , X_{\max} and shower geometry provided by the hybrid reconstruction. Namely, $S_{i,\text{comp}}$ can be directly calculated for each station involved in a hybrid event using as input the hybrid-reconstructed E , X_{\max} and shower geometry while F_{μ} can be derived using the measured signal in a station of the SD, defined as S_{rec} , by reversing Eq. (1) and then fixing $S_{\text{pred}} = S_{\text{rec}}$ as in the following equation:

$$F_{\mu} = \frac{S_{\text{rec}} - \sum_i (1 - \alpha_i) S_{i,\text{comp}}}{\sum_i \alpha_i S_i}. \quad (2)$$

The terms α_i account for the correlation between the i -th component and the muonic component, where the coefficients $\alpha_{\mu} = \alpha_{e\gamma(\mu)} = 1$.

IV. DATASET

This section details the dataset used for the search for UHE primary photons. The presented analysis is based on selected hybrid data collected from 1 January 2005 to 31 December 2017.

We adopted a *blind analysis* approach, which consists in extracting a sub-sample of the data, corresponding to 5% of the total and called *burnt sample*, to define and optimize the analysis performance and to study the expected background for this analysis. The hybrid dataset effectively used in the search for photons, after the subtraction of the burnt sample, amounts to about 2.8 million events.

A. Hybrid data selection

Several selection criteria are applied to ensure a good quality and optimal resolution on reconstructed shower parameters, such as geometry, E and X_{\max} . The event selection is inspired by the strategy adopted for previous hybrid analyses, both for mass composition measurements [21] and for photon searches with hybrid events [22–24]. It is carried out through four levels: pre-selection, geometry, longitudinal profile and quality of the atmosphere.

a. Pre-selection: The initial dataset consists of all events passing the conservative trigger requirements implemented in the data acquisition [10]. Consequently, it still includes events to be removed for this analysis (e.g., lightning or low-energy events with a random-coincidence station). Events are rejected if the reconstruction process failed or if they have been recorded during time periods with known detection system issues (e.g., problems with the communications system or with unstable photomultipliers) or eventually without good FD or SD working conditions mostly occurring during the construction phase of the Observatory.

b. Geometry: To ensure that the probability of a trigger from at least one SD station is unity above 1 EeV regardless of the primary particle type, it is required that the station selected in the hybrid reconstruction is within 1500 m from the shower axis. The angular track length, defined as the angular separation between the highest and lowest elevation FD

pixels in the track, has to be larger than 15° . Events are selected if they land within a maximum distance from the triggered telescope such that the WCD trigger efficiency remains flat within 5% [23, 25] when shifting the energy scale by its systematic uncertainty, i.e. by $\pm 14\%$ [26]. This distance, parameterized in different energy intervals, is based on simulations and is mostly independent of the mass composition and hadronic models. Only events with zenith angle up to 60° are considered for this analysis. More inclined events are not included because the absorption of the electromagnetic components of the air shower in the atmosphere would be too high and the resultant trigger efficiency for photons too small in particular at the lowest energies. As a consequence of these geometrical selection criteria, a resolution of about 40 m in the reconstructed core position and of 0.5° in the determination of the arrival direction are reached for events with energy above 1 EeV.

c. Longitudinal profile: the accuracy in the measurement of the longitudinal profile of a shower affects the resolutions on the reconstructed energy and depth of the shower maximum, X_{\max} . A viewing angle between the shower axis and the telescope larger than 20° is required for rejecting events pointing towards the FD which have a large Cherenkov-light contamination. Biases in the reconstruction of the longitudinal profile are reduced by requiring that the observed X_{\max} is in the telescope field of view and the fraction of gaps in the profile is smaller than 20% of the total observed length. Moreover only events with a relative uncertainty on the calorimetric energy smaller than 20% are accepted. These criteria ensure a resolution of the calorimetric energy at a level of 7 to 8% and a resolution of X_{\max} below 20 g cm^{-2} , in line with the standard Auger analyses [21, 27].

d. Quality of the atmosphere: To exclude reflections or obscuration of fluorescence light by clouds, it is necessary to operate in a clean atmosphere, according to the combined information provided by several monitoring devices installed at the Observatory [11, 12]. In particular, events are rejected if either the sky projection provided by the infrared cloud cameras or the ground-level projection provided by the GOES satellites indicates the presence of clouds over the array. When no data from these monitoring systems are available, the event is accepted only if during the data taking the average cloud fraction reported by Lidars operating at the FD sites is below 25%. Finally, time periods with poor viewing conditions are excluded, requiring that the vertical aerosol optical depth (VAOD), measured by the central laser facilities, integrated from the ground to 3 km is smaller than 0.1.

B. Universality and SD data selection

The minimum requirement for accepting a signal from an SD station participating in a selected hybrid event is assessed using simulations. The simulated showers have been produced using CORSIKA [28] version 7.64, with EPOS-LHC [29] as the model for the description of the hadronic interactions at the highest energies, and FLUKA [30] at lower energies. The showers are generated in the energy and

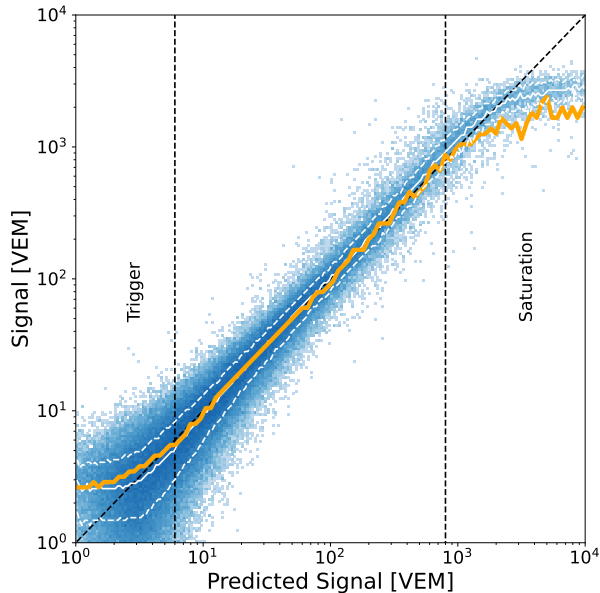


Figure 3. Correlation between reconstructed and predicted signal for EPOS-LHC proton simulations (blue dots) with energies in the range of $10^{17.5}$ eV to $10^{19.5}$ eV. Trigger effects are visible on the left, and saturation effects on the right, both extending beyond the region enclosed by the dashed lines. Hybrid data from the burnt sample are shown on top of simulations (solid orange line).

zenith-angle ranges of interest for this analysis, i.e., between $10^{17.5}$ eV and $10^{19.5}$ eV, with angles between 0° and 65° . The overall simulated data sample consists of about 3 (6) million proton (photon)-initiated events. The simulation and reconstruction pipeline is based on the `Offline` software [31] which combines a detailed simulation of the FD and light propagation through the atmosphere with a GEANT4-based [32] simulation of the SD. The detector response is reproduced accounting for the time-dependent configuration of the Observatory, that is, considering the actual status of the FD and SD data acquisition and the measured conditions of the atmosphere as a function of time, following the approach described in [25].

As shown in Fig. 3, the selection criteria for accepting signals in the SD stations are derived by studying the correlation between the reconstructed and predicted signal, for simulations and for hybrid data. Between 6 and 800 VEM, the accuracy of the parametrization is better than 10%. Biases appear below 6 VEM,¹ due to trigger effects, and above 800 VEM because of saturation effects. Thus, stations are included in the analysis if their signal size is in the range between 6 and 800 VEM. Hybrid data from the burnt sample (solid orange line) agree with expectations at the level of 10% within the selected region.

¹ The signals reconstructed in the SD stations are measured in units of the signal produced by a vertical muon traversing the detector (VEM).

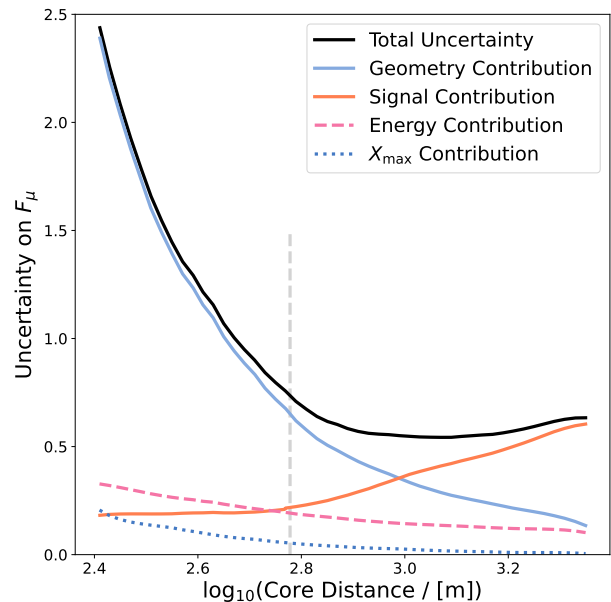


Figure 4. Uncertainty on F_μ , σ_{F_μ} , (black solid line) as a function of the distance to the shower core. The colored lines show the different contributions: signal (orange, solid), geometry (blue, solid), energy (magenta, dashed) and X_{\max} (blue, dotted). The dashed gray vertical line marks the lower edge of the allowed core distance for this analysis (600 m).

The performance of the F_μ calculation is studied as a function of the distance from the shower core by using proton-initiated showers. In particular, as shown in Fig. 4, the overall uncertainty in F_μ at distances less than 600 m (set as lower edge for this analysis) becomes very large and is dominated by the contribution due to the resolution of the geometric reconstruction in combination with the steepness of the air shower lateral distribution close to the axis. Moreover, above 600 m the overall uncertainty on F_μ stabilizes within 15% of its value up to the highest distances. The additional contributions to the overall uncertainty in F_μ (also shown in Fig. 4) are due, on the one hand, to the fluctuations of the signal and, on the other hand, to the reconstruction of the hybrid observables, such as energy and X_{\max} . When more than one station pass the described selection criteria for a given event, an average value of F_μ is calculated by using the individual uncertainty as a weight.

Table I shows the effect of the selection criteria on the data. Overall, out of the 2 990 303 events in the full dataset, 68 886 events are selected while in the simulation samples, the same selection pipeline yields 17 215 proton-initiated events and 22 237 photon-initiated ones.

V. COMBINING FD AND SD OBSERVABLES: THE MVA APPROACH

The selection criteria discussed in Section IV ensure a good resolution of the two key variables for photon/hadron separa-

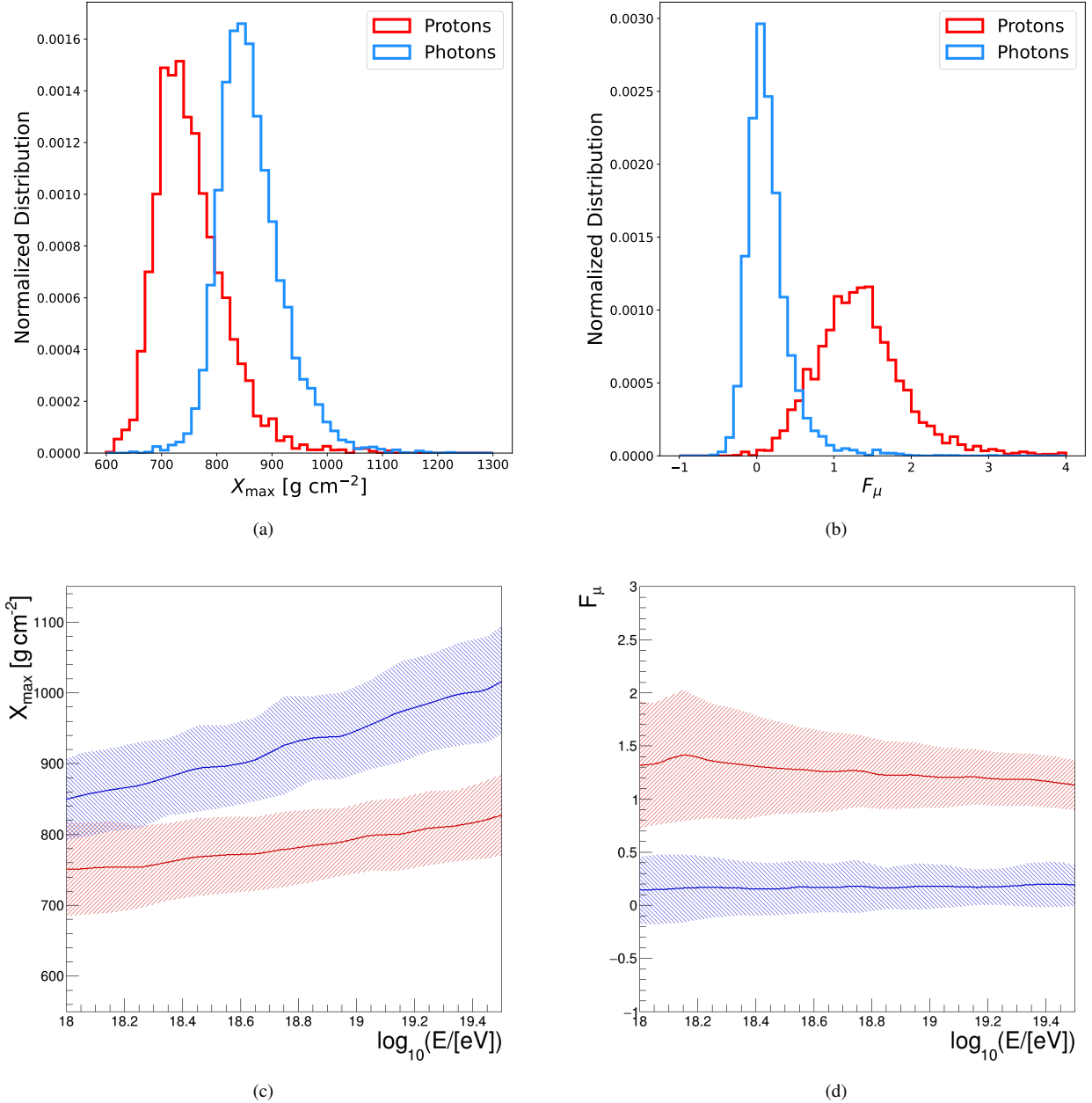


Figure 5. Distributions of the reconstructed X_{\max} (a) and F_{μ} (b) for photon-initiated (blue) and proton-initiated (red) air showers, with energies ranging between 10^{18} eV and $10^{18.5}$ eV. The evolution of the average X_{\max} and F_{μ} with respect to energy are shown in panel (c) and (d) for protons (red) and photons (blue). The shaded areas enclose one standard deviation.

tion, X_{\max} and F_{μ} . Their distributions are shown in panels (a) and (b) of Fig. 5, respectively, for photon (signal) and proton (background) initiated showers within the energy range from $10^{18.0}$ eV to $10^{18.5}$ eV. These simulations are re-weighted assuming a power-law energy distribution $dN/dE \propto E^{-\Gamma}$ with spectral index $\Gamma = 2.7$ for protons and $\Gamma = 2.0$ for photons, motivated by previous Auger photon searches [23, 34]. Panels (c) and (d) illustrate the dependence of X_{\max} and F_{μ} on energy. Overall, the discussed variables provide an excellent separation power between the considered primary species.

While the separation power for this analysis is comparable to that used in [23], the F_{μ} -based criterion provides a selection efficiency that improves with energy, exceeding that used in [23] above 2.5 EeV and reaching 100% at the highest energies. Furthermore, F_{μ} is almost independent of the primary particle energy, whereas X_{\max} shows a logarithmic dependence on the energy.

The performance of the combined observables in terms of photon/hadron separation is expected to surpass that of each variable separately, as illustrated in panel (a) of Fig. 6. The

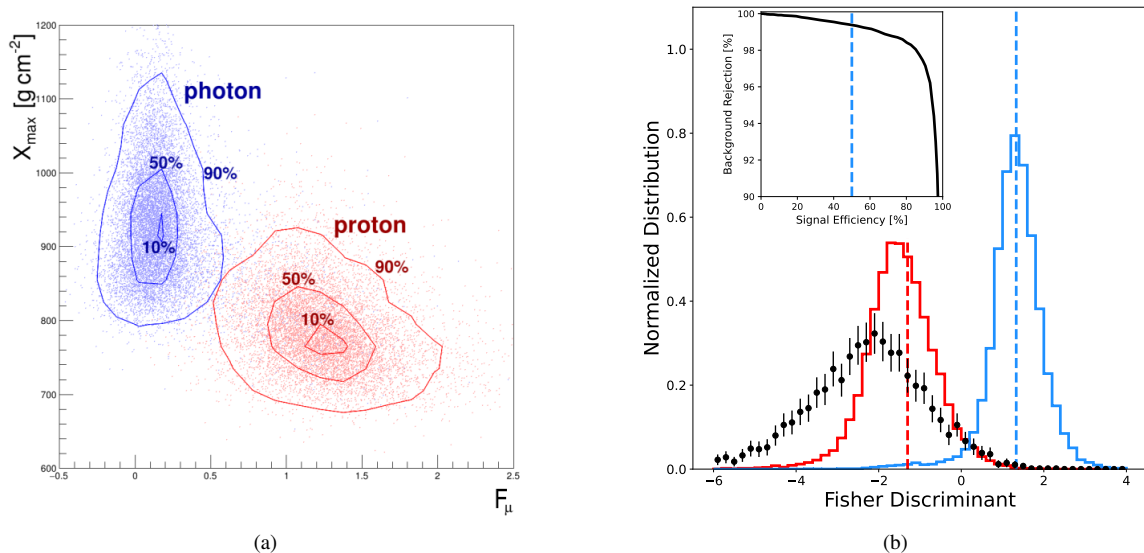


Figure 6. **(a)**: X_{\max} - F_{μ} distributions for photons (blue) and protons (red). Contour lines enclose the 90%, 50% and 10% of the distributions of the events, re-weighted to a realistic power law spectrum $E^{-\Gamma}$ ($\Gamma = 2.7$ for protons and $\Gamma = 2.0$ for photons) [33]. **(b)**: Distribution of the Fisher discriminant for simulated photons (signal, blue) and protons (background, red), and for the burnt sample (black). The vertical red line indicates the value of the Fisher discriminant ($f = -1.3$) above which the background begins to decrease nearly exponentially, while the photon selection efficiency is still very close to 100%; the blue line indicates the median of the photon distribution. **(Inset)**: background rejection as a function of signal efficiency obtained with the Fisher Discriminant Analysis.

	N	ε (%)
Raw Sample	2 990 303	
Pre-selection	1 103 316	36.9
Geometry	393 651	35.7
Profile	198 933	50.5
Atmosphere	133 741	67.2
Universality	68 886	51.5

Table I. Hybrid data: event selection criteria, number of events at different selection levels with the cut efficiency ε , calculated with respect to the preceding cut. See text for details on the definition of the selection levels.

blue (red) contour lines enclose 90%, 50% and 10% of the photon (proton) distributions. They have clearly separated peaks, with minimal overlapping tails. The F_{μ} and X_{\max} parameters do not show any significant degree of correlation.

To maximize the potential of the hybrid approach, F_{μ} is then combined with X_{\max} within the framework of a multivariate analysis (MVA). The dependence of the two variables on the energy is also taken into account as an additional parameter. In the following, the variable defined as $E_{\gamma} = (1 + 1\%) E_{\text{cal}}$ will be used as an estimator for the primary (photon) energy. E_{cal} is the calorimetric shower energy reconstructed by the FD and the factor 1% accounts for the invisible energy contribution due to neutrinos and high-energy muons ending underground [35]. E_{γ} will be used as default for simulations and data, independently of the nature of the primary particle.

More specifically, a Fisher discriminant analysis [36] was

performed, using three input parameters, F_{μ} , X_{\max} and $\log_{10}(E_{\gamma})$ combined linearly to obtain a Fisher discriminant, f . The event classification is then made in the transformed f space. The linear discriminant analysis identifies an axis in the hyperspace of the input variables such that, when projecting the output classes (signal and background) along this axis, the separation between the two classes is maximized, while the dispersion of the simulated events within each class is minimized. The use of a Fisher discriminant analysis is an appropriate choice for this case as it provides a robust event classification for uncorrelated input observables, which is the case for F_{μ} and X_{\max} . In addition to that, the discriminant can be calculated analytically for each event. In Fig. 6 (b), the distribution of the Fisher discriminant is shown for simulated photons (blue) and protons (red), along with data from the burnt sample (black). The vertical red line indicates the value of the Fisher discriminant ($f = -1.3$) above which the background begins to decrease nearly exponentially, while the photon selection efficiency is still very close to 100%; the blue line indicates the median of the photon distribution. Assuming photons as signal and proton as background, the background rejection power as a function of signal efficiency is shown in the inset panel of Fig. 6 (b). As an example, for a signal efficiency of 50% (dashed blue line), a background rejection at the level of 99.75% is achieved.

VI. BACKGROUND EXPECTATION

For this analysis, the expected amount of background is calculated from data. Firstly, the distribution of the Fisher dis-

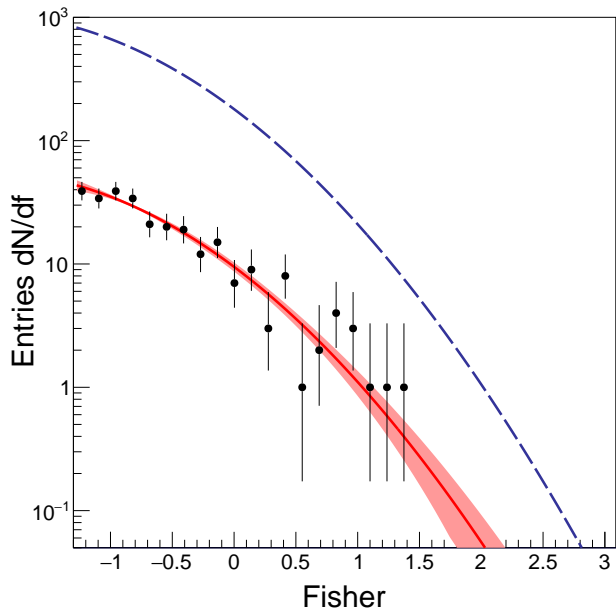


Figure 7. Distribution of the Fisher discriminant for the burnt sample (black points), together with the fit to the m function (red line) and the 1σ uncertainty (red band). The dashed blue line shows the background expected in the full hybrid data sample.

criminant f has been parameterised above the value $f = -1.3$ introduced in section V. The shape of the distribution has been modeled based on proton simulations, assuming an exponential function m defined as

$$m(f|A, B) = N(A, B)e^{-(Af^2+Bf)}, \quad (3)$$

where A and B are shape parameters and N is a normalization factor, calculated by requiring that the integral of m above -1.3 equals the number of events in the burnt sample in the same range of f . The fit of the Fisher distribution to the burnt data is shown in Fig. 7 as a red line superimposed to data points.

A possible photon contamination in the burnt sample cannot be excluded: a related systematic effect has thus been studied by using a jackknife technique [37]. This is a re-sampling technique, which involves a leave-one-out strategy for the estimation of the parameters (in this case, A and B) in a data set of n observations. A detailed description of the background estimate, along with the values of the parameters A and B and the corresponding uncertainties is given in the Appendix A.

The distribution of the Fisher discriminant for the extrapolated background is shown as a blue line in Fig. 7 along with its 1σ uncertainties included as a blue band.

The extrapolation of the background is thus used to determine the optimal value of the Fisher discriminant cut, f_γ , for selecting photon candidates. The upper limit values can be optimized by following the approach described in [38], in the case of signal non-observation. In this way, f_γ has been found to be approximately at the median of the Fisher discriminant

distribution for photons. The median value ($f_\gamma \simeq 1.4$, blue vertical line in Fig. 6), has been adopted as photon candidate cut. Finally, the number of expected false-positive events in the full hybrid data set can be calculated by integrating the function describing the extrapolated background above f_γ , and it yields 30 ± 15 .

VII. PHOTON SEARCH IN DATA

The method is applied to the full hybrid data sample that, after the application of the selection criteria described in Section IV, results in 68 886 hybrid events of which 26 752 have E_γ above 10^{18} eV.

The distribution of f , obtained by combining X_{\max} and F_μ in the dataset, is displayed in Fig. 8 (a) where the vertical dashed blue line represents the photon selection cut. In Fig. 8 (b) the tail of the Fisher distribution ($f > -1.3$), enclosing ~ 5600 events (black points), is shown along with the shaded blue bands representing the expected background, with uncertainties at different sigma levels.

As one can see, the data distribution is compatible with that from the expected background. The median selection cut yields 22 candidates, which is well-consistent with the expectation of 30 ± 15 false-positive candidates, as calculated in the previous section. The general characteristics of the candidate events are summarised in Table II, where E_γ , X_{\max} , F_μ , the UTC time and the value of the Fisher discriminant are reported for each candidate.

The candidate event with the highest Fisher value has the peculiarity of having a very deep X_{\max} . The event, labeled with the ID 3478968 was detected on 22 May 2007 at 02:58:14 UTC. The atmospheric conditions at the time of the event were checked and found to be optimal, with a measured VAOD of 0.02 and no cloud coverage. The hybrid reconstruction yields an energy $E_\gamma = (1.73 \pm 0.16) \times 10^{18}$ eV, a depth of the shower maximum $X_{\max} = (1245 \pm 57)$ g cm $^{-2}$ and a zenith angle $\theta = (56.7 \pm 1.0)^\circ$. The footprint of the event on the SD array is characterized by six triggered stations. Out of them, only three stations pass the selection criteria for the calculation of F_μ described in Section IV. The station with the largest signal size is, in fact, rejected because it is too close to the core, while the other two excluded stations are rejected because of their small signal size. The F_μ associated with this event is 0.75 ± 0.41 . By combining it with the value of X_{\max} , the resulting value of the Fisher discriminant is $f \simeq 2.87$.

The event was also cross-checked with SD-based information. Namely, the risetime of the signals in the triggered stations has been analysed and found to be consistent with an event developing late in the atmosphere.

To study more in detail this specific candidate, 2000 proton showers, characterised by the same geometric configuration and energy as the candidate, were simulated (see Fig. 9) with CORSIKA using EPOS-LHC as the model for high-energy hadronic interaction. It turns out that only three proton events (blue dots) lie beyond the photon cut at the energy of the candidate but none out the 2000 ones exhibit a Fisher value larger than that of the candidate (blue cross), namely $f_c = 2.87$.

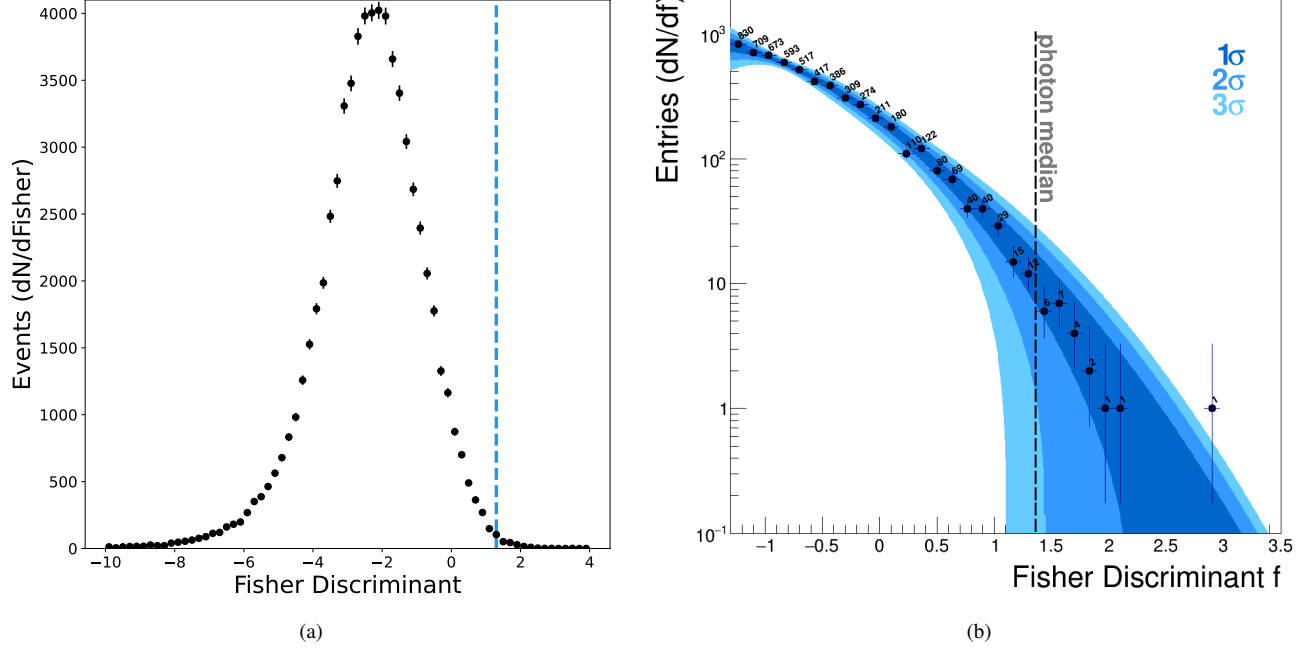


Figure 8. **a:** Fisher discriminant distribution of the selected hybrid data sample; **b:** Tail of the Fisher discriminant distribution ($f > -1.3$) of the hybrid data sample (black dots). The vertical dashed line represented the photon-median cut. The shaded blue areas show the 1, 2, 3 σ uncertainties in the expected background.

UTC time	$\lg(E_\gamma/\text{eV})$	$X_{\text{max}}/(\text{g cm}^{-2})$	F_μ	$\theta/^\circ$	Fisher
Jun 22, 2006 07:27:16	18.31	987.7	0.42	38.7	1.57
Jun 27, 2006 03:01:26	18.01	1039.9	0.39	47.6	2.12
May 22, 2007 02:58:14	18.24	1245.2	0.75	56.7	2.87
Aug 10, 2007 03:05:06	18.02	907.6	0.22	43.6	1.46
Dec 15, 2007 06:29:00	18.00	913.4	0.29	47.8	1.40
Mar 26, 2009 06:34:56	18.10	938.9	0.11	39.0	1.84
Oct 19, 2009 06:54:20	18.29	1008.7	0.52	47.8	1.57
Oct 21, 2009 03:51:13	18.01	1010.4	0.59	59.3	1.58
Jan 19, 2010 03:55:42	18.21	796.3	-0.23	22.7	1.36
Oct 03, 2010 05:07:00	18.01	1019.9	0.52	49.6	1.75
Oct 16, 2010 07:33:46	18.14	984.7	0.45	47.3	1.57
Jun 26, 2011 05:17:41	18.17	935.6	0.07	30.8	1.86
Jul 05, 2011 06:17:13	18.02	1109.3	1.01	57.2	1.57
Aug 03, 2011 01:59:06	18.20	944.3	0.20	54.6	1.68
Dec 22, 2011 05:31:33	18.08	932.7	0.02	44.2	1.96
Nov 13, 2012 06:51:13	18.04	967.5	0.48	35.0	1.45
Jun 30, 2013 02:01:08	18.04	1061.8	0.86	41.7	1.47
Mar 15, 2015 06:32:28	18.48	1001.9	0.45	51.8	1.55
Mar 08, 2016 01:23:38	18.04	954.3	0.29	54.5	1.67
Jul 05, 2016 06:01:34	18.12	917.0	0.07	48.1	1.74
Aug 11, 2016 07:52:15	18.07	847.4	0.01	58.5	1.38
Jun 19, 2017 01:14:36	18.05	849.9	-0.07	42.4	1.54

Table II. Details of the events selected by the photon candidate cut.

The probability to observe a background event with the same zenith angle and energy that yields to a Fisher value larger than f_c is consequently $< 1/2000$. However, because X_{max} and F_μ can combine to form a Fisher value larger than f_c for showers whose zenith angle and energy lie anywhere in the pa-

rameter space explored in the analysis (“look-elsewhere” effect [39]), this probability is only *local*. To quantify the compatibility between the selected candidate and a background event *globally*, we have then simulated a large number of showers to probe the entire parameter space. 100,000 reali-

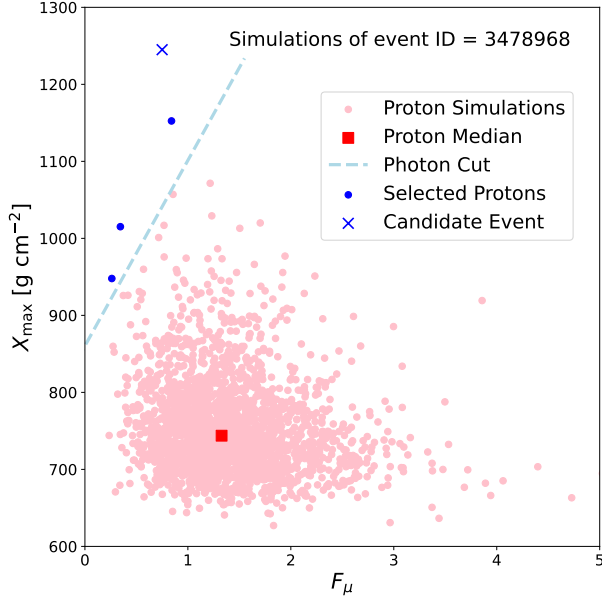


Figure 9. Simulation of 2000 proton showers with the same energy, geometry and detector configuration as the most significant candidate event with ID 3478968 (blue cross). The reconstructed X_{\max} and F_{μ} of the simulated events are shown as light red dots. The light blue dashed line shows the photon cut at the energy of the candidate event. Three out of them are selected as false-positive photon candidates (blue circles).

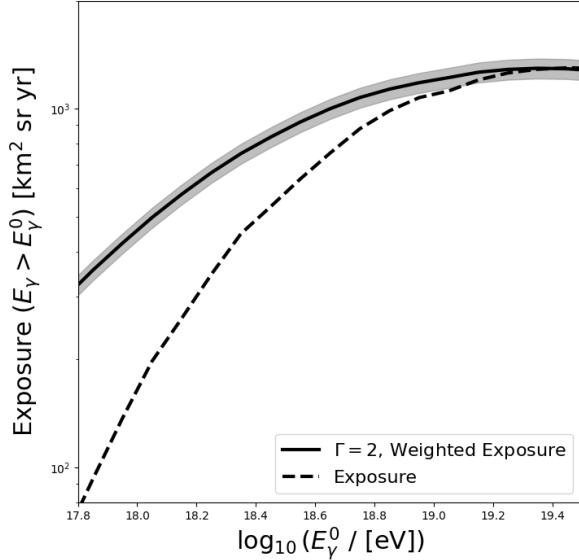


Figure 10. Weighted hybrid exposure for primary photons (solid line) in the time interval from 1 January 2005 to 31 December 2017, assuming a power-law spectrum with $\Gamma = 2$. Systematic uncertainties due to the on-time and the trigger efficiency are shown as a gray band. The raw exposure (dashed line) is also shown for comparison.

sations of the data sample using the extrapolated Fisher distribution have been generated as a background model. The p -value characterising the deviation of f_c from the background model is obtained by counting the number of realisations with $\max(f) > f_c$ out of the total. It amounts to 25%, which gives a very modest overall significance for claiming that the candidate is a photon.

VIII. PHOTON FLUX UPPER LIMITS

Since no significant excess of photons has been observed with respect to the background, upper limits on the diffuse UHE photon flux, $\Phi_{\gamma}^{\text{C.L.}}$, are derived as

$$\Phi_{\gamma}^{\text{C.L.}}(E_{\gamma} > E_{\gamma}^0) = \frac{N_{\gamma}^{\text{C.L.}}(E_{\gamma} > E_{\gamma}^0)}{\mathcal{E}_{\gamma}(E_{\gamma} > E_{\gamma}^0)} \quad (4)$$

where $N_{\gamma}^{\text{C.L.}}$ is the upper limit on the number of photons at a certain confidence level above an energy threshold E_{γ}^0 , and \mathcal{E}_{γ} is the weighted hybrid exposure to photons above the same E_{γ}^0 .

A. The hybrid photon exposure

The raw exposure of the hybrid detector to photons is calculated following the approach detailed in [25], as

$$\mathcal{E}_{\gamma} = \int dt \int d\Omega \cos \theta \int dS \varepsilon_{\gamma}(E_{\gamma}, t, \theta, \phi, x, y), \quad (5)$$

where ε_{γ} is the overall photon efficiency, including detection, reconstruction, and selection of events. ε_{γ} is a function of zenith angle θ , azimuth angle ϕ , impact position x, y , time t and energy, E_{γ} .

The raw exposure \mathcal{E}_{γ} is then weighted with a power law spectrum assuming a spectral index $\Gamma = 2$, namely

$$\mathcal{E}_{\gamma}^{\text{weighted}}(E_{\gamma} > E_{\gamma}^0) = \frac{\int_{E_{\gamma}^0}^{\infty} E_{\gamma}^{-\Gamma} \mathcal{E}_{\gamma}(E_{\gamma}') dE_{\gamma}'}{\int_{E_{\gamma}^0}^{\infty} E_{\gamma}^{-\Gamma} dE_{\gamma}}. \quad (6)$$

The resulting behavior of $\mathcal{E}_{\gamma}^{\text{weighted}}$ as a function of the energy threshold is shown as a solid line in Fig. 10. The grey shaded band represents the contribution to the systematic uncertainty due to on-time and trigger efficiency, estimated at the level of $\pm 6.4\%$ [23].

B. Upper limits

The calculation of upper limits is carried out through Eq. (4) for five different energy thresholds, E_{γ}^0 , the same as in [23]. They are listed in the first column of Table III.

The values of $N_{\gamma}^{95\%}$ (shown in the fifth column of the table) are computed for each specified threshold as the Rolke [51] upper limit at 95% C.L. of the observed number of photon

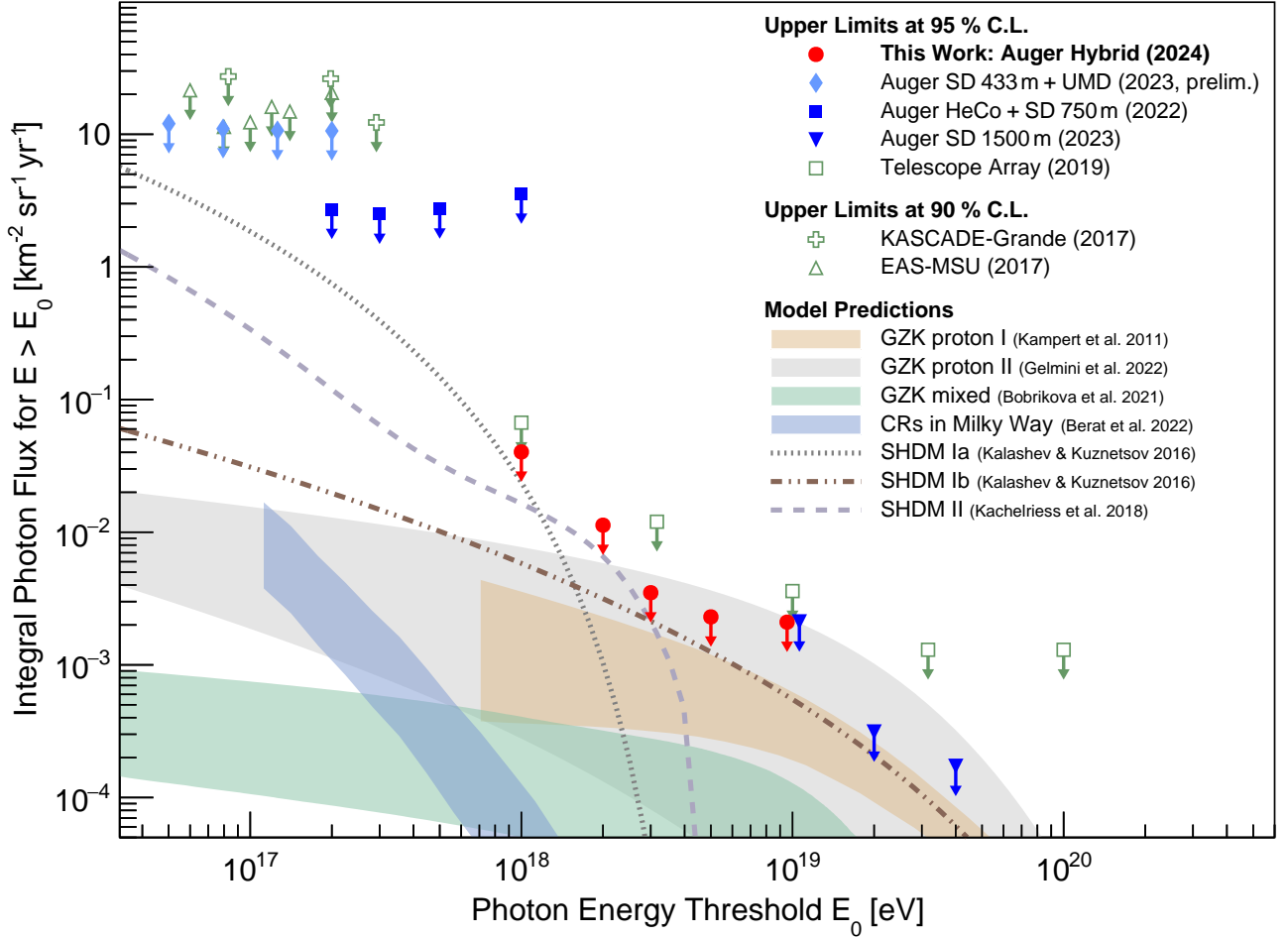


Figure 11. Current upper limits on the integral photon flux determined with data collected by the Pierre Auger Observatory (solid markers) from [24, 40] and preliminary limits from [41]. Additionally, we display upper limits reported by other experiments: KASCADE-Grande (green crosses) [42], EAS-MSU (green triangles) [43], and Telescope Array surface detector (green squares) [44]. The ranges of expected GZK photon fluxes under the assumption of two different pure-proton scenarios are depicted as the brown and gray bands (adapted from [45] and [46], respectively). The water green band illustrates the expected GZK photon flux, assuming a mixed composition that aligns with Auger data [47], while the light blue band signifies the range of photon fluxes expected from cosmic-ray interactions with matter in the Milky Way [48]. Additionally, the expected photon fluxes from the decay of super-heavy dark matter particles for different masses and lifetimes are included [49, 50], see text for more details.

candidates listed in the fourth column. In this calculation, the expected number of background events and its largest uncertainty, reported in the second and third columns respectively, is derived from the parameterisation of the background given in Section VI, after normalizing it to the number of hybrid events above each E_γ^0 . The weighted exposure $\mathcal{E}_\gamma^{\text{weighted}}$ is displayed in the sixth column.

The integral flux upper limits can also be converted into photon fractions upper limits, relative to the measured cosmic rays flux [26], thus leading to 0.15%, 0.21%, 0.15%, 0.26%, 0.77% above the corresponding energy thresholds given in the first column of Table III.

The limits derived from different analyses published by the Pierre Auger collaboration, as well as those published by other cosmic ray observatories, are illustrated in Fig. 11. For comparison, in Fig. 11 the expected fluxes of ultra-high-energy

photons based on different assumptions are also presented. Expectations for two distinct pure-proton scenarios [45, 46] are plotted, along with a scenario involving a mixed composition at the sources [47]. While experimental sensitivities above 3×10^{18} eV are approaching or already constraining the optimistic expectations for the photon flux produced by the interaction of protons during propagation, they remain approximately 1 to 1.5 orders of magnitude above those derived for the mixed-composition model.

Previous upper limits on the photon flux have constrained non-acceleration models, especially Super-Heavy Dark Matter (SHDM) models attempting to elucidate the origin of cosmic rays at the highest energies (see, e.g., [23, 40]). The upper limits on the incoming photon flux allow for the constraint of the mass and lifetime phase space of SHDM particles [6–8]. In Fig. 11, expectations for three distinct assumptions

E_γ^0 (EeV)	$N_b(E_\gamma > E_\gamma^0)$	$N_\gamma(E_\gamma > E_\gamma^0)$	$N_\gamma^{95\%}(E_\gamma > E_\gamma^0)$	$\mathcal{E}_\gamma^{\text{weighted}}(E_\gamma > E_\gamma^0)$ (km ² sr yr)	$\Phi_\gamma^{95\%}(E_\gamma > E_\gamma^0)$ (km ⁻² sr ⁻¹ yr ⁻¹)
1	30_{-15}^{+15}	22	23.38	579	0.0403
2	6_{-2}^{+6}	2	9.53	840	0.0113
3	$0.7_{-0.62}^{+1.9}$	0	3.42	976	0.0035
5	$0.06_{-0.06}^{+0.25}$	0	2.59	1141	0.0023
10	$0.02_{-0.02}^{+0.06}$	0	2.62	1263	0.0021

Table III. Upper limits on the integral diffuse flux of UHE photons (last column). The different energy thresholds are listed in the first column. The following columns refer to the expected number of background events N_b along with its uncertainty σ_b , the number of photon candidates N_γ , the 95% upper limits and the weighted exposure.

regarding SHDM decay are displayed. For the hadronic decay ($X \rightarrow q\bar{q}$), expected fluxes are shown according to [49] for SHDM particle masses (M_X) of 10^{18} GeV with a lifetime (τ_X) of 3×10^{21} yr, as well as for $M_X = 10^{12}$ GeV with $\tau_X = 10^{23}$ yr, both combinations are currently within permissible bounds. Considering the decay into leptons, the expected flux according to [50] is presented for $M_X = 10^{10}$ GeV with $\tau_X = 3 \times 10^{21}$ yr. With the increasing sensitivity of current photon searches, further constraints on these values become achievable.

C. Systematic Uncertainties

Various sources of systematic uncertainties in the calculated upper limits were investigated. The main contributions can be attributed to the systematic uncertainties on the energy scale [26] and on the X_{max} reconstruction [21]. In particular, shifting all energy values upward or downward by 14%, the number of candidates changes by $_{-8}^{+5}$ above the lowest energy threshold of 1 EeV, and by $_{-1}^{+3}$ above 2 EeV, while there is no change for the higher energy thresholds. Similarly, shifting the reconstructed X_{max} values by $\Delta X_{\text{max}} = \pm 10$ g cm⁻² the number of candidates changes by $_{-2}^{+6}$ above 1 EeV, while the higher energy intervals are not affected. The discussed systematic shifts would have a similar impact on the expected background, as it is extrapolated from the burnt sample. The influence of these systematic uncertainties on photon selection efficiency was also evaluated, leading to a contribution of about 5% from the uncertainties on the energy scale and $\sim 14\%$ from the uncertainties on the X_{max} reconstruction. The systematic uncertainty in the calculation of the hybrid exposure, estimated at the level of 6.4% (see Section VIII A), would propagate linearly into an additional systematic uncertainty on upper limits.

Another source of uncertainty is the unknown photon spectral index, which would reflect into a change in the exposure. Differences of 15% and 20% are found in the first two energy intervals when changing the spectral index from 2 to 1.5 and 2.5, respectively. The lack of knowledge of Γ may also have an impact on the analysis, because a different spectral index changes the shape of the distributions used as input vari-

ables for the MVA method. However, in the case of the Fisher Discriminant Analysis, the impact of the change in shape has been found to be negligible compared to the exposure effect.

The choice of a hadronic interaction model can significantly impact the differentiation between photons and protons, given that various models provide unique predictions for X_{max} and the number of muons in showers initiated by hadronic primaries. The uncertainties inherent in modeling proton- and nucleon-induced air showers, which are pivotal for our analysis, may consequently influence the Fisher discriminant analysis. In this study, we employed EPOS-LHC as the designated hadronic interaction model. Air showers generated using this model exhibit the highest substantial muon component and the deepest X_{max} when compared to alternative models. This particular characteristic leads to more conservative upper limits, as illustrated in [23]. The effects of a different hadronic model have been investigated by considering Sybill 2.3c simulations. Notably, we observed a variation of the upper limits of -14% , -8% , -6% , -2% , and $+2\%$ at 1, 2, 3, 5, and 10 EeV, respectively.

IX. CONCLUSIONS

In this study, we performed a search for EeV photons using the full hybrid data sample collected by the Pierre Auger Observatory. The analysis combines the depth at the shower maximum, X_{max} , directly measured from the Observatory's fluorescence detector, with a parameter related to the muonic component of a shower, F_μ , derived from signals of the surface detector, exploiting the air-shower universality paradigm.

The photon selection identified 22 candidates, consistent with the expected background and its uncertainty. This result, summarized in Table III, establishes the most stringent upper limits on the diffuse UHE-photon flux above various energy thresholds. The limits, determined at a 95% confidence level, are 0.0403, 0.01113, 0.0035, 0.0023, and 0.0021 km⁻² sr⁻¹ yr⁻¹ at 1, 2, 3, 5, and 10 EeV, respectively.

Compared to previous analyses [23], the reported upper limits exhibit a substantial improvement, up to a factor of ~ 3 in the energy region above 3 EeV, where no candidates were found and the background is compatible with zero.

This result can be attributed to an increase of about 50% in measurement time in combination with a near doubling of the event selection efficiency, leading to a three-fold increase of the exposure. Remarkably, the upper limit above 10 EeV turns out to be at the level of the limit obtained with the surface detector in the corresponding energy range [40]. Finally, the enhancement above the lowest energy threshold is about 40%, primarily attributed to the inclusion of a background estimate in the calculation of the upper limits.

While the current limits do not challenge the flux of photons produced during the propagation of UHECRs under the assumption of a mixed composition, they begin to probe the most optimistic predictions of pure-proton scenarios. Moreover the upper limits on the incoming photon flux allow for the constraint of the mass and lifetime phase space of super-heavy dark matter particles. Finally, the analysis presented in this study can serve as a complementary method for directional searches from specific targets or searches in coincidence with observations from other cosmic messengers such as neutrinos and/or gravitational waves. Future data will enhance the ability to constrain different mechanisms expected to produce UHE photons. Specifically, the completion of the upgrade of the Pierre Auger Observatory, AugerPrime [52, 53], is expected to further increase the sensitivity of the analysis.

Appendix A: Background estimation

The goal of this section is to describe the distribution of the Fisher discriminant for the background. This is achieved in two steps as shown in [38]. In the first step, we study its shape by profiting of the statistics offered by the proton simulations. Only the rightmost tail of the Fisher distribution is considered, specifically only the events with a Fisher discriminant $f > -1.3$, indicated by the blue vertical line in Fig. 8a. This value of the Fisher discriminant is used because below $f_0 = -1.3$ the photon selection efficiency is almost 100%.

The tail of the proton distribution is highlighted in Fig. 12, where two exponential functions, m' and m , tested for its description, are superimposed (black dashed and solid lines, respectively):

$$m'(f|B) = N'(B)e^{-Bf} \quad (\text{A1a})$$

$$m(f|A, B) = N(A, B)e^{-(Af^2+Bf)} \quad (\text{A1b})$$

where A and B are shape parameters, and N' and N are the normalizations of m' and m , respectively. N' and N are calculated as a function of the parameters A and B , by requiring that the integral of m' and m is equal to the number of events N_0 that have a value of the Fisher discriminant above f_0 , thus obtaining

$$N'(A) = \frac{N_0 B}{e^{-Bf_0}} \quad (\text{A2a})$$

$$N(A, B) = \frac{N_0 \sqrt{A}}{e^{B^2/4A} \operatorname{erfc}\left(\frac{B}{2\sqrt{A}}\left(\frac{2A}{B}f_0 - 1\right)\right)} \quad (\text{A2b})$$

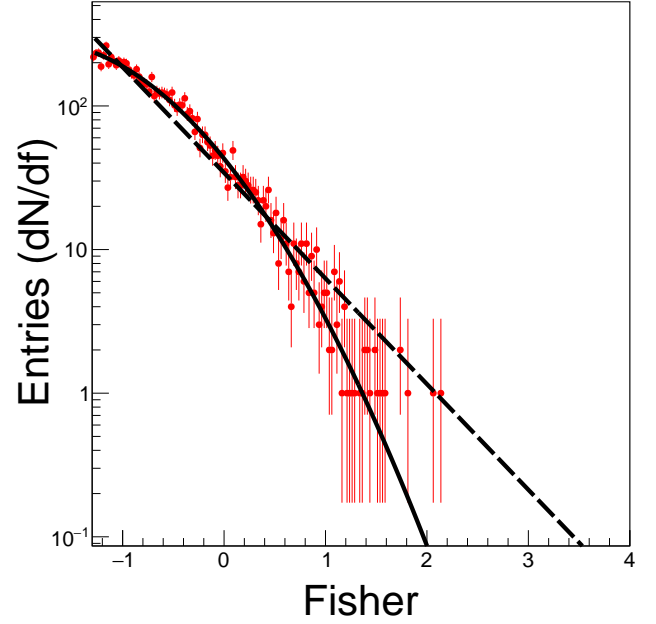


Figure 12. Tail of the Fisher distribution for protons. The two black lines represent the fits of the two functions, m' (dashed) and m (solid), discussed in the text.

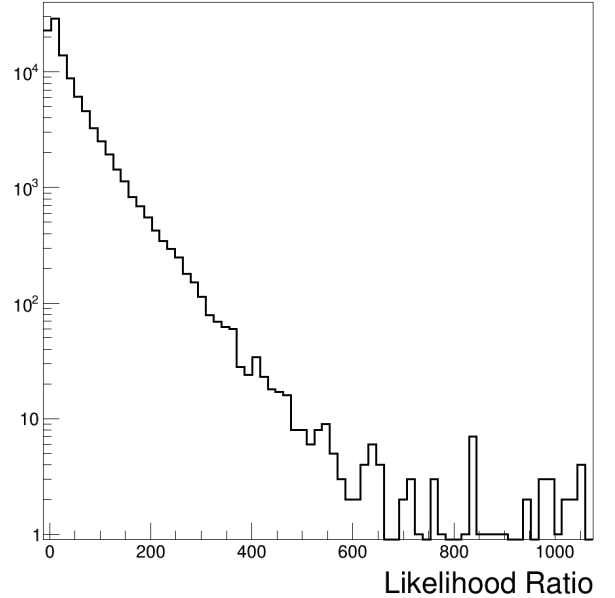


Figure 13. Likelihood-ratio distribution from the fit of m' and m to 10^6 simulated samples (see text for details).

where erfc is the complementary error function. The parameters obtained from an unbinned likelihood fit of m' and m to the tail of the Fisher distribution are reported in Table IV.

The best-fit model is determined by using a likelihood-ratio test [54], in which two hypotheses on the shape of the tail distribution are compared: the null-hypothesis, H_0 , according to which it is described by m' , i.e., $m'(f|B) = m(f|A = 0, B)$; the

	A	B
m'	1.55	
m	0.42	-1.73

Table IV. Values of the parameters A and B obtained from an unbinned likelihood fit to the tail of the Fisher distribution of protons, i.e., to events with $f > -1.3$.

alternative hypothesis, H_1 , according to which it is described by $m(f|A \neq 0, B)$. The likelihood ratio $\mathcal{L}_{\text{ratio}}$ results to be ≈ 4000 . The p-value, p_{value} , associated to $\mathcal{L}_{\text{ratio}}$ is derived by applying the likelihood-ratio test on simulated samples of Fisher values, generated according to the m' model and then fitted with both models. Each sample consists of 30000 events (*realizations*). The resulting distribution of the likelihood-ratios, based on 1 000 000 realizations, is shown in Fig. 13. As the maximum value attained in 10^6 trials is about 1000, i.e., $p_{\text{value}}(1000) \approx 10^{-6}$, then $p_{\text{value}} < 10^{-6}$, i.e., the m' model is discarded in favor of m .

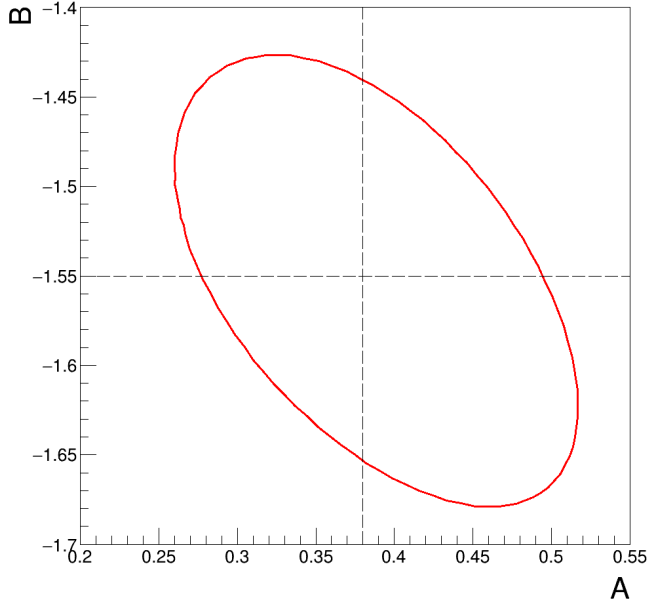


Figure 14. 1-sigma contour plot of the errors of the parameters A and B . The dashed lines indicate the values obtained from the fit of m on the burnt sample.

After having derived the shape of the background from proton simulations, the second step in the characterisation of the background involves the burnt sample. To finalize the estimation of the background, a fit with the m model is performed on the burnt sample distribution, as shown in Fig. 7 (see Section VI). The best-fit values of A and B are 0.38 and -1.55 , respectively: they are represented by the grey dashed lines in Fig. 14, together with the red ellipses that marks the 1-sigma contour of the statistical errors.

A possible photon contamination in the burnt sample cannot however be excluded: a possibly related systematic ef-

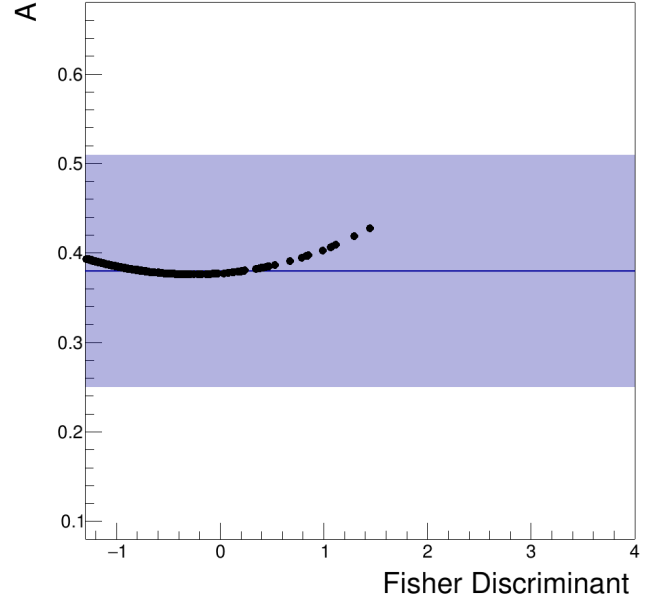


Figure 15. Parameter A as calculated with the jackknife technique (see text), as a function of the Fisher discriminant. The blue line shows the values obtained from the fit on the burnt sample, while the blue shaded area show the statistical uncertainties.

fect has thus been studied by using a jackknife technique [55]. This is a re-sampling technique, which involves a leave-one-out strategy for the estimation of the parameters (in this case, A and B) in a data set of N observations. The values of A and B calculated as a function of the Fisher discriminant f with this technique are shown in Fig. 15 and Fig. 16, respectively. The blue shaded area represents the statistical uncertainties obtained from the fit. As one can see, the systematic deviations from the central values (marked by the blue lines) are negligible with respect to the statistical ones. A systematic uncertainty of 0.01 is then derived from the width of the distribution of the deviations when projected on the y-axis.

The parameters of the burnt sample obtained from the fit of the model m to the burnt sample distribution are thus:

$$A = 0.38 \pm (\text{stat}) 0.13 \pm (\text{syst}) 0.01 \quad (\text{A3a})$$

$$B = -1.55 \pm (\text{stat}) 0.13 \pm (\text{syst}) 0.01 \quad (\text{A3b})$$

Finally, to extrapolate the parametrisation of the Fisher distribution of the background to the full hybrid data set, the normalization of the function m is scaled to the number of total events by setting $N = N_{\text{data}}$ in Eq. (A2b), where $N_{\text{data}} = 1328$. The distribution of the Fisher discriminant for the extrapolated background is shown as a blue line in Fig. 7. The uncertainties, σ_f , in the extrapolation, represented by the blue band, is calculated as

$$\sigma_f = \sum_{i,j=A,B} \frac{\partial m}{\partial i} k_{ij} \frac{\partial m}{\partial j} \quad (\text{A4})$$

where i and j runs over the parameters A and B , and k_{ij} are the

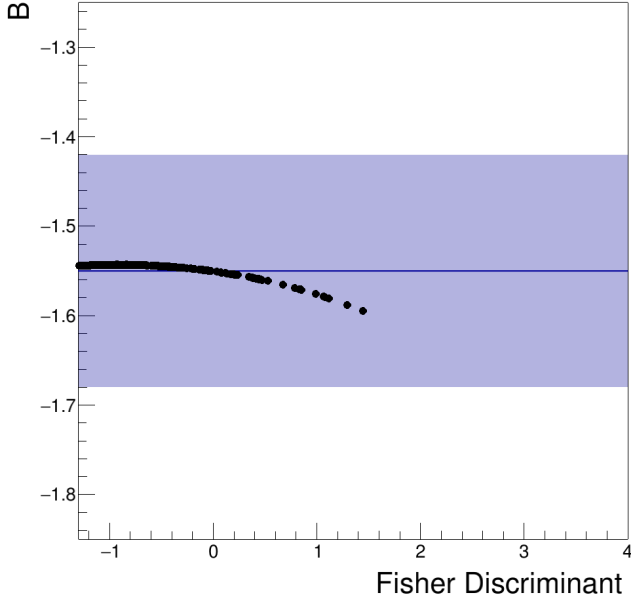


Figure 16. Parameter B as calculated with the jackknife technique (see text), as a function of the Fisher discriminant. The blue line shows the values obtained from the fit on the burnt sample, while the blue shaded area show the statistical uncertainties.

elements of the covariance matrix:

$$K = \begin{pmatrix} 0.0165 & -0.0086 \\ -0.0086 & 0.0158 \end{pmatrix} \quad (\text{A5})$$

Appendix B: The most significant photon candidate event

In this appendix the characteristics of the most significant photon candidate event (ID 3478968, see [Section VII](#), and [Table II](#)) are discussed in detail. The event has occurred on 22 May 2007, arriving at a zenith angle of about 57° and with reconstructed energy $E_\gamma = (1.73 \pm 0.16) \times 10^{18}$ eV, and $X_{\max} = (1245 \pm 57)$ g cm $^{-2}$.

The hybrid event, detected with both the surface and fluorescence detectors simultaneously, triggered 6 stations of the ground array, providing independent SD trigger and reconstruction. The FD telescope, Los Leones, observed the event that triggered 14 pixels, with a total angular track of around 17 degrees. The event passed all the selection criteria of the analysis and had the highest Fisher value in the data sample, 2.87.

In [Fig. 17](#), left panel, the 3D visualization of the event at the Observatory is provided. The fluorescence telescopes are represented by colored squares, the ground array stations are marked with gray dots. The line of sight of the triggered FD pixels looking towards the reconstructed shower axis are shown as colored lines, and the circles show the positions of the triggered SD stations. Colors reflect triggering times: violet corresponds to early and red to late times. The camera view of the FD telescope detecting the event is shown in [Fig. 17](#), top

right panel: the horizontal axis corresponds to the azimuth angle in the FD site local system while the vertical axis is the angular elevation of the viewing direction of the FD pixels. Same color code for triggering times, gray pixels are background triggered pixels not participating in the event geometry reconstruction. The energy deposit as a function of the traversed atmospheric slant depth is shown in [Fig. 17](#), bottom right panel. The fit to the shower longitudinal profile (red solid line) and its uncertainty (red band) are shown in the Figure along with the position of the shower maximum and its uncertainty (red point).

ACKNOWLEDGMENTS

The successful installation, commissioning, and operation of the Pierre Auger Observatory would not have been possible without the strong commitment and effort from the technical and administrative staff in Malargüe. We are very grateful to the following agencies and organizations for financial support:

Argentina – Comisión Nacional de Energía Atómica; Agencia Nacional de Promoción Científica y Tecnológica (ANPCyT); Consejo Nacional de Investigaciones Científicas y Técnicas (CONICET); Gobierno de la Provincia de Mendoza; Municipalidad de Malargüe; NDM Holdings and Valle Las Leñas; in gratitude for their continuing cooperation over land access; Australia – the Australian Research Council; Belgium – Fonds de la Recherche Scientifique (FNRS); Research Foundation Flanders (FWO), Marie Curie Action of the European Union Grant No. 101107047; Brazil – Conselho Nacional de Desenvolvimento Científico e Tecnológico (CNPq); Financiadora de Estudos e Projetos (FINEP); Fundação de Amparo à Pesquisa do Estado de Rio de Janeiro (FAPERJ); São Paulo Research Foundation (FAPESP) Grants No. 2019/10151-2, No. 2010/07359-6 and No. 1999/05404-3; Ministério da Ciência, Tecnologia, Inovações e Comunicações (MCTIC); Czech Republic – GACR 24-13049S, CAS LQ100102401, MEYS LM2023032, CZ.02.1.01/0.0/0.0/16.013/0001402, CZ.02.1.01/0.0/0.0/18.046/0016010 and CZ.02.1.01/0.0/0.0/17.049/0008422 and CZ.02.01.01/00/22_008/0004632; France – Centre de Calcul IN2P3/CNRS; Centre National de la Recherche Scientifique (CNRS); Conseil Régional Ile-de-France; Département Physique Nucléaire et Corpusculaire (PNC-IN2P3/CNRS); Département Sciences de l’Univers (SDU-INSU/CNRS); Institut Lagrange de Paris (ILP) Grant No. LABEX ANR-10-LABX-63 within the Investissements d’Avenir Programme Grant No. ANR-11-IDEX-0004-02; Germany – Bundesministerium für Bildung und Forschung (BMBF); Deutsche Forschungsgemeinschaft (DFG); Finanzministerium Baden-Württemberg; Helmholtz Alliance for Astroparticle Physics (HAP); Helmholtz-Gemeinschaft Deutscher Forschungszentren (HGF); Ministerium für Kultur und Wissenschaft des Landes Nordrhein-Westfalen; Ministerium für Wissenschaft, Forschung und Kunst des Landes Baden-Württemberg; Italy – Istituto Nazionale di Fisica Nucleare (INFN); Istituto Nazionale di Astrofisica (INAF);

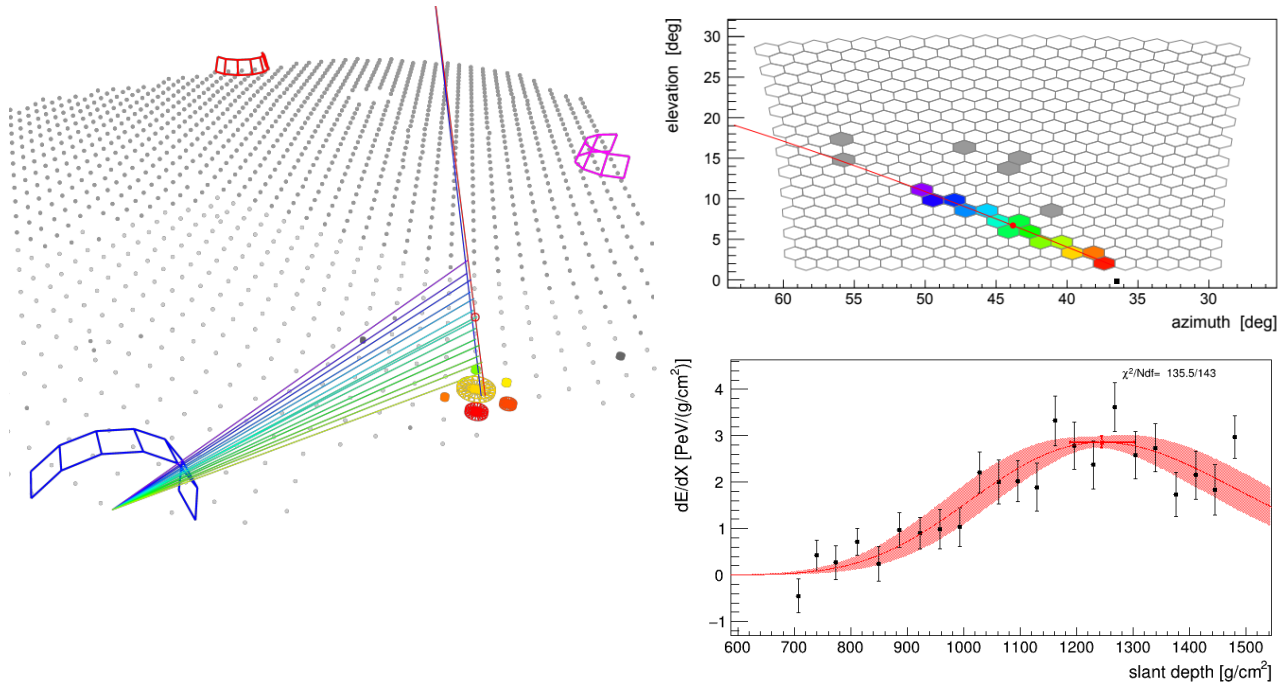


Figure 17. Characteristics of the most significant photon candidate event, ID 3478968: 3D visualization (left panel), camera view of the triggered FD telescope (top right panel). The colors (violet to red) reflect the times (early to late) at which the light reaches each pixel. Gray pixels indicate background triggered pixels. Bottom right panel, reconstructed energy deposit as a function of atmospheric slant depth (black points) along with the fit to the shower longitudinal profile (red line).

Ministero dell'Università e della Ricerca (MUR); CETEMPS Center of Excellence; Ministero degli Affari Esteri (MAE), ICSC Centro Nazionale di Ricerca in High Performance Computing, Big Data and Quantum Computing, funded by European Union NextGenerationEU, reference code CN_00000013; México – Consejo Nacional de Ciencia y Tecnología (CONACYT) No. 167733; Universidad Nacional Autónoma de México (UNAM); PAPIIT DGAPA-UNAM; The Netherlands – Ministry of Education, Culture and Science; Netherlands Organisation for Scientific Research (NWO); Dutch national e-infrastructure with the support of SURF Cooperative; Poland – Ministry of Education and Science, grants No. DIR/WK/2018/11 and 2022/WK/12; National Science Centre, grants No. 2016/22/M/ST9/00198, 2016/23/B/ST9/01635, 2020/39/B/ST9/01398, and 2022/45/B/ST9/02163; Portugal – Portuguese national funds and FEDER funds within Programa Operacional Factores de Competitividade through Fundação para a Ciência e a Tecnologia (COMPETE); Romania – Ministry

of Research, Innovation and Digitization, CNCS-UEFISCDI, contract no. 30N/2023 under Romanian National Core Program LAPLAS VII, grant no. PN 23 21 01 02 and project number PN-III-P1-1.1-TE-2021-0924/TE57/2022, within PNCDI III; Slovenia – Slovenian Research Agency, grants P1-0031, P1-0385, I0-0033, N1-0111; Spain – Ministerio de Ciencia e Innovación/Agencia Estatal de Investigación (PID2019-105544GB-I00, PID2022-140510NB-I00 and RYC2019-027017-I), Xunta de Galicia (CIGUS Network of Research Centers, Consolidación 2021 GRC GI-2033, ED431C-2021/22 and ED431F-2022/15), Junta de Andalucía (SOMM17/6104/UGR and P18-FR-4314), and the European Union (Marie Skłodowska-Curie 101065027 and ERDF); USA – Department of Energy, Contracts No. DE-AC02-07CH11359, No. DE-FR02-04ER41300, No. DE-FG02-99ER41107 and No. DE-SC0011689; National Science Foundation, Grant No. 0450696; The Grainger Foundation; Marie Curie-IRSES/EPLANET; European Particle Physics Latin American Network; and UNESCO.

- [1] K. Greisen, *Phys. Rev. Lett.* **16**, 748 (1966).
 [2] G. T. Zatsepin and V. A. Kuzmin, *JETP Lett.* **4**, 78 (1966).
 [3] S. Lee, *Phys. Rev. D* **58**, 043004 (1998).
 [4] T. K. Gaisser, *Cosmic Rays and Particle Physics* (Cambridge University Press, 1990).
 [5] F. Halzen, *Nature Phys.* **13**, 232 (2017).

- [6] L. A. Anchordoqui *et al.*, *Astroparticle Physics* **132**, 102614 (2021).
 [7] P. Abreu *et al.*, *Phys. Rev. D* **107**, 042002 (2023).
 [8] P. Abreu *et al.* (The Pierre Auger Collaboration), *Phys. Rev. Lett.* **130**, 061001 (2023).
 [9] L. D. Landau and I. Pomeranchuk, *Dokl. Akad. Nauk Ser. Fiz.*

- 92, 535 (1953); 92, 735 (1953); A. B. Migdal, *Phys. Rev.* **103**, 1811 (1956).
- [10] A. Aab *et al.* (The Pierre Auger Collaboration), *Nucl. Instrum. Meth. A* **798**, 172 (2015), arXiv:1502.01323 [astro-ph.IM].
- [11] P. Abreu *et al.* (The Pierre Auger Collaboration), *Journal of Instrumentation* **7**, P09001 (2012).
- [12] V. Harvey *et al.* (The Pierre Auger Collaboration), *PoS ICRC2019*, 283 (2019).
- [13] M. Unger, B. Dawson, R. Engel, F. Schüssler, and R. Ulrich, *Nucl. Instrum. Meth. A* **588**, 433 (2008).
- [14] A. Aab *et al.* (The Pierre Auger Collaboration), *Journal of Cosmology and Astroparticle Physics* **03**, 018 (2019), arXiv:1811.04660 [astro-ph.HE].
- [15] A. Aab *et al.* (The Pierre Auger Collaboration), *Phys. Rev. D* **100**, 082003 (2019).
- [16] T. Bergmann, R. Engel, D. Heck, N. Kalmykov, S. Ostapchenko, T. Pierog, T. Thouw, and K. Werner, *Astroparticle Physics* **26**, 420 (2007).
- [17] S. Lafebre, R. Engel, H. Falcke, J. Hörandel, T. Huege, J. Kuipers, and R. Ulrich, *Astroparticle Physics* **31**, 243 (2009).
- [18] L. Cazon, R. Conceição, and F. Riehn, *Journal of Cosmology and Astroparticle Physics* **2023**, 022 (2023).
- [19] M. Ave, R. Engel, M. Roth, and A. Schulz, *Astroparticle Physics* **87**, 23 (2017).
- [20] M. Ave, M. Roth, and A. Schulz, *Astroparticle Physics* **88**, 46 (2017).
- [21] A. Aab *et al.* (The Pierre Auger Collaboration), *Phys. Rev. D* **90**, 122005 (2014), arXiv:1409.4809 [astro-ph.HE].
- [22] J. Abraham *et al.* (The Pierre Auger Collaboration), *Astropart. Phys.* **31**, 399 (2009), arXiv:0903.1127 [astro-ph.HE].
- [23] A. Aab *et al.* (The Pierre Auger Collaboration), *Journal of Cosmology and Astroparticle Physics* **2017**, 009 (2017); *Journal of Cosmology and Astroparticle Physics* **2020**, E02 (2020).
- [24] P. Abreu *et al.* (The Pierre Auger Collaboration), *Astrophys. J.* **933**, 125 (2022), arXiv:2205.14864 [astro-ph.HE].
- [25] P. Abreu *et al.* (The Pierre Auger Collaboration), *Astropart. Phys.* **34**, 368 (2011), arXiv:1010.6162 [astro-ph.HE].
- [26] A. Aab *et al.* (The Pierre Auger Collaboration), *Phys. Rev. D* **102**, 062005 (2020), arXiv:2008.06486 [astro-ph.HE].
- [27] B. Dawson *et al.* (The Pierre Auger Collaboration), *PoS ICRC2019*, 231 (2019).
- [28] D. Heck, J. Knapp, J. N. Capdevielle, G. Schatz, and T. Thouw, *CORSIKA: A Monte Carlo code to simulate extensive air showers* (Forschungszentrum Karlsruhe Report, 1998).
- [29] K. Werner, *Nuclear Physics B - Proceedings Supplements* **175-176**, 81 (2008).
- [30] A. Ferrari, P. R. Sala, A. Fasso, and J. Ranft, *CERN Yellow Reports* (2005).
- [31] S. Argirò *et al.*, *Nucl. Instrum. Meth. A* **580**, 1485 (2007).
- [32] S. Agostinelli *et al.* (GEANT4 Collaboration), *Nucl. Instrum. Meth. A* **506**, 250 (2003).
- [33] P. Savina (The Pierre Auger Collaboration), *PoS ICRC2021*, 373 (2021).
- [34] A. Aab *et al.* (The Pierre Auger Collaboration), *The Astrophysical Journal* **789**, 160 (2014); *The Astrophysical Journal Letters* **837**, L25 (2017).
- [35] T. Pierog, R. Engel, and D. Heck, *Czechoslovak Journal of Physics* **56**, A161 (2006), 51.53.01; LK 02; Suppl.A.
- [36] R. Fisher, *Annals of Eugenics* **7**, 179 (1936).
- [37] B. Efron and C. Stein, *The Annals of Statistics* **9**, 586 (1981).
- [38] P. Savina, *Search for gamma-rays in the EeV sky at the Pierre Auger Observatory using universality*, Ph.D. thesis, IJCLab, Orsay, INFN, Italy, Università del Salento, Université Paris-Saclay (2021).
- [39] L. Lyons, *The Annals of Applied Statistics* **2**, 887 (2008).
- [40] P. Abreu *et al.* (The Pierre Auger Collaboration), *Journal of Cosmology and Astroparticle Physics* **05**, 021 (2023).
- [41] N. González *et al.* (The Pierre Auger Collaboration), *PoS ICRC2023*, 238 (2023).
- [42] W. D. Apel *et al.*, *The Astrophysical Journal* **848**, 1 (2017).
- [43] Y. A. Fomin, N. N. Kalmykov, I. S. Karpikov, G. V. Kulikov, M. Y. Kuznetsov, G. I. Rubtsov, V. P. Sulakov, and S. V. Troitsky, *Phys. Rev. D* **95**, 123011 (2017).
- [44] R. Abbasi *et al.*, *Astroparticle Physics* **110**, 8 (2019).
- [45] B. Sarkar, K.-H. Kampert, and J. Kulbartz, in *32nd International Cosmic Ray Conference*, Vol. 2 (2011) p. 198.
- [46] G. B. Gelmini, O. Kalashev, and D. Semikoz, *Universe* **8**, 402 (2022).
- [47] A. Bobrikova, M. Niechciol, M. Risse, and P. Rühl, *PoS ICRC2021*, 449 (2021).
- [48] C. Bérat, C. Bleve, O. Deligny, F. Montanet, P. Savina, and Z. Torrès, *The Astrophysical Journal* **929**, 55 (2022).
- [49] O. E. Kalashev and M. Y. Kuznetsov, *Phys. Rev. D* **94**, 063535 (2016).
- [50] M. Kachelrieß, O. E. Kalashev, and M. Y. Kuznetsov, *Phys. Rev. D* **98**, 083016 (2018).
- [51] W. A. Rolke, A. M. López, and J. Conrad, *Nucl. Instrum. Meth. A* **551**, 493 (2005).
- [52] A. Aab *et al.* (The Pierre Auger Collaboration), “The pierre auger observatory upgrade - preliminary design report,” (2016), arXiv:1604.03637 [astro-ph.IM].
- [53] A. Castellina *et al.* (The Pierre Auger Collaboration), *EPJ Web Conf.* **210**, 06002 (2019).
- [54] L. Lista, *Statistical Methods for Data Analysis in Particle Physics*, Vol. 909 (Springer, 2016).
- [55] B. Efron and C. Stein, *The Annals of Statistics* **9**, 586 (1981).